Experimental Verification of a Two-Dimensional Inverse Method for Turbidity Currents Using a Deep Neural Network

Seiya Fujishima¹, Hajime Naruse¹

¹Kyoto University
¹Division of Earth and Planetary Sciences, Graduate School of Science, Kyoto University, Kyoto, Japan

Key Points:

10

11

12

13

- We developed horizontal two-dimensional inverse models for turbidity currents using deep neural networks.
- The models successfully reconstructed flow conditions from the observed characteristics of experimental turbidites.
- The proposed inverse modeling approach is applicable to field-scale turbidity currents over complex deep-sea topography.

Corresponding author: Seiya Fujishima, fujishima.seiya.78w@st.kyoto-u.ac.jp

Abstract

14

15

16

18

19

20

21

22

23

24

25

26

27

28

30

31

32

34

35

36

37

38

39

41

42

43

45

46

47

48

49

50

51

52

53

54

55

56

57

61

62

Turbidites have been widely studied as indicators of the occurrences and magnitudes of paleo-tsunamis and paleo-earthquakes. Inversion to estimate the flow conditions from turbidites offers valuable i nsights i nto the magnitudes of paleo-seismic and t sunami events. However, conventional one-dimensional inverse models are insufficient for capturing the behavior of turbidity currents in tectonically active margins, where the seafloor topography is typically complex. Here, we developed a horizontal two-dimensional inverse model of turbidity currents based on a deep neural network (DNN) and evaluated its performance using both synthetic and flume experiment datasets. The model's uccessfully estimated the model input parameters with a symmetric mean absolute percentage error (SMAPE) of less than 32.5%, except for the density-equivalent sediment concentration for saline water at the inlet. When applied to experimental data, the model reasonably reconstructed the flow c onditions, y ielding S MAPE v alues between 5 1.7 a nd 8 6.2%, despite the potential uncertainties introduced by sampling disturbances, data processing, and forward model limitations. The spatial distribution of bed thickness was also well predicted, except in cases where most of the suspension bypassed the depositional zone. Overall, the proposed inverse model demonstrated accuracy comparable to the previous one-dimensional model while offering g reater applicability to c omplex s eafloor geometries and maintaining low computational costs. These results suggest that the proposed method is well-suited for the field-scale inversion of turbidity currents in realistic geological settings.

Plain Language Summary

Turbidity currents are sediment-laden flows that transport material from shallow marine environments to the deep-sea floor. These flows are often triggered by natural disasters such as earthquakes and tsunamis. Understanding the magnitude of turbidity currents is therefore essential for reconstructing the size and frequency of past seismic and tsunami events. In this study, a deep neural network model was developed to estimate the scale of turbidity currents propagating over complex seafloor to pography. The model's performance was evaluated using both synthetic and experimental datasets. The results demonstrate that the model can accurately estimate turbidity current magnitudes with low computational cost. This deep learning approach holds promise for estimating the scale of ancient turbidity currents in deep-sea environments and, in turn, for improving assessments of the recurrence intervals of large earthquakes and tsunamis.

1 Introduction

Turbidity currents are sediment-gravity flows driven by the excess density of suspended sediment supported by fluid turbulence. Turbidity currents are the primary mechanism supplying sediment to the deep sea floor (Piper et al., 1999; Talling et al., 2012) and are known to form large-scale submarine topography such as submarine canyons and submarine fans (Kuenen & Migliorini, 1950).

Turbidites, the deposits of turbidity currents, are widely recognized as valuable archives of past geohazard events, as those currents can be triggered by various catastrophic phenomena, including storms, river floods, ort s unamis. For instance, A rai et al. (2013) estimated that the tsunami-induced turbidity current sociated with the 2011 Tohoku-Oki earthquake had an exceptional scale, extending a rarea at least 90 km wide and 100 km long. The head velocity of this flow ranged from 2.4–7.1 m/s, and the maximum velocity in the flow body was estimated to be 8.0 m/s. Polonia et al. (2013) reported that the 365 AD Cretan mami ($M_{\rm w}$ 8.3–8.5) generated a turbidity current that resulted in a widely distributed turbidite (about 375 km) and thick turbidite (1.84 m). In the 1929 Grand Banks earthquake, which has $M_{\rm w}$ of 7.2±0.3 (Bent, 1995), a landslide triggered a large-scale turbidity current with estimated velocity of 19 m/s and greater than 150 km³



64

65

68

69

70

71 72

73

74

75

76

77

78

80

81

82

83

84

85

86

88

89

90

91

92

93

94

95

97

100

101

102

103

104

105

106

108

109

110

111

112

113

114

115

116

sediment transport (Piper & Aksu, 1987). Hsu et al. (2008) reported that the 2006 Pingtung earthquake in Taiwan ($M_{\rm w}$ 7.0) generated a turbidity current with velocity 3.7–20.0m/s. Reconstructing the flow conditions of such earthquake- or tsunami-induced turbidity currents offers the potential to infer past large-scale earthquakes, thereby contributing to our understanding of long-term risks of geohazards.

Therefore, the quantitative estimation of the flow conditions of ancient turbidity currents remains a major challenge in sedimentary and geohazard research (e.g., Komar, 1985; Hiscott, 1994). Because these flow events cannot be directly observed, researchers must rely on inverse analysis from their resulting deposits. Falcini et al. (2009), for example, applied a forward model of turbidity currents based on the shallow water equation to the Lower Messinian Laga Formation in Italy and performed inverse analysis. However, their approach assumed a steady-state flow to derive an analytical solution, limiting its applicability to turbidites formed under unsteady flow conditions. In contrast, Lesshafft et al. (2011) developed an inverse model using a direct simulation as the forward model, coupled with the surrogate management method for parametric optimization. Although their method achieved reasonable accuracy when tested on synthetic data, its high computational load renders it impractical for field-scale applications. Parkinson et al. (2017) proposed a more computationally efficient approach using a one-dimensional shallow-water turbidity current model and the adjoint method. Their inverse model, applied to the Miocene Marnoso-arenacea Formation in Italy, yielded initial flow heights of 3950 m under a uniform grain-size assumption and 0.00192 m for a two-size-class assumption. These values are difficult to reconcile with realistic flow conditions. More recently, Nakao et al. (2020) employed a genetic algorithm as the optimization method for inverse analysis of a turbidite in the Kiyosumi Formation, Boso Peninsula, Japan. Although their model produced more plausible flow conditions, the model reliability could not be tested because of the high computational load of the repeated forward model calculations. A common limitation across these studies is the substantial computational burden of inverse modeling, which often involves repeated forward simulations that are difficult to parallelize. This constraint hampers the systematic evaluation of model accuracy across multiple synthetic or real-world datasets.

To overcome these limitations, Naruse and Nakao (2021) recently proposed an inverse analysis framework based on deep learning. Their approach comprises two primary steps. First, a large training dataset is generated by a numerical simulation of turbidity currents under randomly sampled initial conditions. Unlike the iterative forward calculations required in conventional inverse modeling, this data generation process is inherently parallelizable, significantly reducing computational costs. Second, a fully connected deep neural network (DNN) is trained to learn the relationship between the initial flow conditions and the resulting deposit characteristics, such as the thickness and grain size distributions. Once trained, the DNN serves as an efficient inverse model capable of instantly predicting the initial conditions from the observable features of unknown turbidites. This method avoids the need for simplifying assumptions in the forward model and simultaneously achieves high inversion accuracy with reduced computational demand. The trained DNN's rapid prediction capability further enables systematic validation of inversion performance using a large number of test datasets. Cai and Naruse (2021) validated this methodology and demonstrated its effectiveness in estimating initial conditions from both synthetic 1D data and flume experiments. Furthermore, this deep learning-based framework has also been extended to the analysis of tsunami deposits, successfully estimating tsunami inundation depths and deposit characteristics in agreement with field observations (Mitra et al., 2020, 2021, 2024).

Despite the significant progress achieved through DNN-based inversion methods, a key limitation remains. Previous studies have primarily employed one-dimensional (or vertically vo-dimensional) forward models, which are only applicable to turbidity currents occurring in flat, laterally uniform sedimentary basins or submarine channels. Conse-

quently, these models cannot be readily extended to environments with complex, undulating bathymetry, such as deep-sea fans. An attempt to address this limitation was made by Cai (2022), who developed a horizontally two-dimensional inverse model using a DNN and applied it to turbidites observed in the Anno Formation of the Awa Group. However, the proposed method has not yet been validated against known flow conditions. Since direct measurements of ancient turbidity currents are unavailable, it is essential to compare model predictions with well-constrained flume experiments to assess the accuracy and reliability of newly proposed inverse models (Cai & Naruse, 2021).

In response to these challenges, this study aims to develop a horizontal two-dimensional inverse model based on DNNs and to validate its performance using flume experiment data. First, the inverse model was trained and tested on synthetically generated datasets to evaluate its baseline performance. Second, flume experiments simulating turbidity currents were conducted to obtain detailed measurements of flow conditions—including velocity, flow height, suspended sediment concentration, and duration—as well as the resulting bed thickness and the grain-size distribution. Finally, the trained inverse models were applied to the experimental turbidites and to datasets from the preventation, and their accuracy was evaluated by comparing the predicted flow parameters with the corresponding measured values.

2 Methods

2.1 Flume Experiments

Flume experiments were performed to verify the performance of the inverse models. Two experimental series were conducted under different conditions for this purpose. All of these experiments were conducted using the experimental flume at the Graduate School of Science, Kyoto University (Figure 1). The flume was 4.5 m long, 2.2 m wide, and 1.8 m deep. A during tank was installed at the downstream end to prevent the reflection of turbidity currents. During the experiment, the water was drained from the dumpin and at the downstream end to keep the water level in the flume constant. Plastic (melamine) particles were used in these experiments. The particle density was $1490 \,\mathrm{kg/m^3}$. Sediment and salt water (only in Experimental Series 1) were mixed in mixing tanks (0.45 m³) using propellers and a pump. A diffuser pipe with a diameter of 0.06 m and a length of 0.61 m was installed as a flow inlet at the upstream end. In total, 22 holes with a diameter of 5.0×10^{-3} mm were opened on the side of the pipe. The acrylic cover, which is 0.30 m long, 0.64 m wide, and 0.20 m high, was installed at the inlet (Figure 1). This cover was slightly moved from the inlet due to the jet in Run 2 of the Experimental Series 1. The sediment-water mixtures were injected from the mixing tanks using a pump. The non-erodible plastic plate 1.9 m wide and 4.5 m long was installed in the flume. The slope was set to 10% from the inlet to 1.2 m downstream, and 5% to the downstream end.

2.1.1 Experimental settings

In Series 1, two runs were conducted. Run 1 was performed over the initial flat topography, and Run 2 was performed over the deposit formed in Run 1. In Series 1, salt water was used to increase the flow density, which approximates fine materials (i.e., clays) in actual turbidity currents. The flow discharge in the pipe connected to the inlet was kept constant at $3.0 \times 10^{-3} \,\mathrm{m}^3/\mathrm{s}$. The durations of Runs 1 and 2 of Series 1 were 116 and 113 seconds for Runs 1 and 2, respectively. The total volumetric concentration in the mixing tanks C_{tank} was 3.76% and 3.04% in Runs 1 and 2, respectively. The density of salt water in the mixing tanks was 1060 kg/m³ in both Runs 1 and 2 of Series 2 (Table 1). The flow discharge was expected to rapidly increase at the inlet due to the entrainment of ambient water around the injection jets, resulting in the dilution of the suspended sediment. The mean and standard deviation of the grain size in the mixing

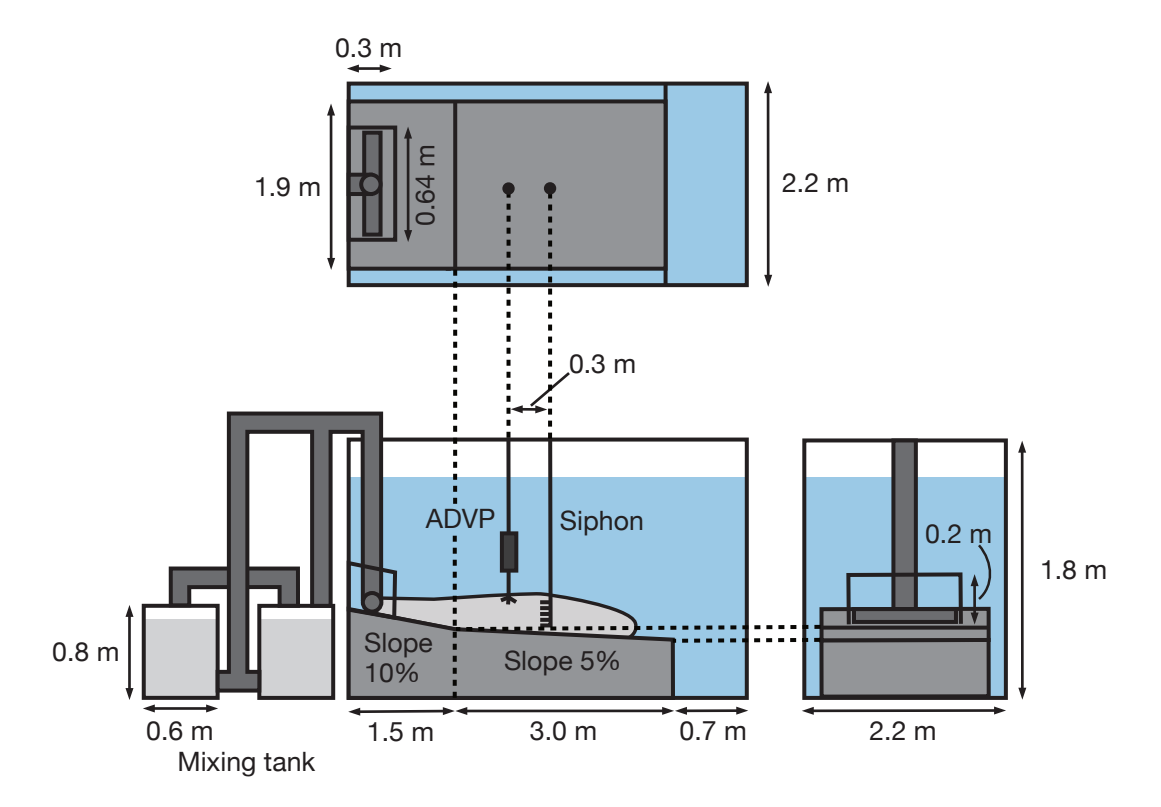


Figure 1. Schematic diagram of the experimental setup in Series 1 and 2 conducted in this study.



tank were $1.6\times10^{-4}\,\mathrm{m}$ and $6.8\times10^{-4}\,\mathrm{m}$, respectively, in Run 1 in Series 1; and $1.2\times10^{-4}\,\mathrm{m}$ and $5.8\times10^{-4}\,\mathrm{m}$ in Run 2 in Series 1 (Figure 2). The initial topography and sediment composition of Series 2 were the same as those of Series 1. This series also comprised two runs. As in Series 1, Run 1 flowed over the initial flat topography, and Run 2 flowed over the topography formed by Run 1. The mixtures of fresh water and plastic particles were released into the flume using a pump. The property of the discharge was constant at $1.4\times10^{-3}\,\mathrm{m}^3/\mathrm{s}$ in Run 1, and $2.0\times10^{-3}\,\mathrm{m}^3/\mathrm{s}$ in Run2. The flow durations were 279 and 230 seconds for Runs 1 and 2, respectively. The total volumetric concentration in impring tanks was 4.96% and 4.41% in Runs 1 and 2, respectively. The mean grain size and standard deviation of particles in the mixing tank were $1.8\times10^{-4}\,\mathrm{m}$ and $6.6\times10^{-4}\,\mathrm{m}$ in Run 1 of Series 2; and $1.4\times10^{-4}\,\mathrm{m}$ and $5.8\times10^{-4}\,\mathrm{m}$ in Run 2 in Series 2. (Figure 2). The inverse analysis was performed only for Run 2 because the velocity data could not be obtained in Run 1 of Series 2.

2.1.2 Measurement of flow conditions

This study measured flow velocity using the acoustic Doppler velocimetry (ADV) Nortek Vectrino and the acoustic Doppler velocity profiler (ADVP) Nortek Vectrino Profiler. The ADVP used in this study can measure the flow velocity in a vertical range of 0.03 m with a resolution of 1 mm, whereas the ADV can only measure the velocity at a single point. Both facilities were moved vertically during the experiments using an electric actuator to cover the entire flow velocity profile. The velocity data were time-averaged over at least 15 seconds each.

Table 1. Experimental condition of Series 1 and Series 2 conducted in this study.

Series 1	Run 1	Run 2
Concentration in the mixing tank Density of salt water (kg/m³) Density of sediment particle (kg/m³) Temperature (°C)	0.0376 1060 1490 16.3	0.0304 1060 1490 14.8
Series 2	Run 1	Run 2
Concentration in the mixing tank Density of sediment particle (kg/m ³) Temperature (°C)	0.0496 1490 22.0	0.0441 1490 24.7

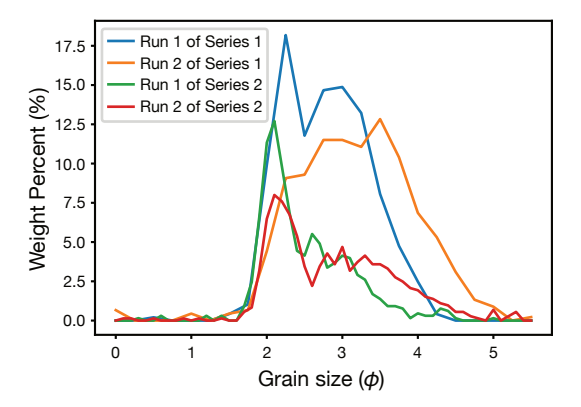


Figure 2. Grain-size distribution of sediment used in Series 1 and Series 2 conducted in this study. The sediment was sampled from the mixing tank before each run.

In Series 1, flow velocity measurements were conducted at the center in the value had direction and 2.1 m from the upstream end in the longitudinal direction (Figure 3). The ADV measured the flow velocity in Run 1 of Series 1, moving vertically every 0.03 m to measure the velocity profile from the bottom to 0.18 m above the bed. In Run 2 of Series 2, the ADVP was used to measure the flow velocity profile. The vertical ranges measured in this run were 0–0.03 m, 0.02–0.05 m, 0.08–0.11 m, and 0.14–0.17 m above the bed. In Series 2, the flow velocity profile was also obtained using the ADVP at the center in the width direction and 1.2 m from the upstream end in the longitudinal direction. Flow velocities were measured in this run at 0–0.02 m, 0.01–0.04 m, 0.03–0.06 m, and 0.07–0.10 m above the bed (Figure 3).

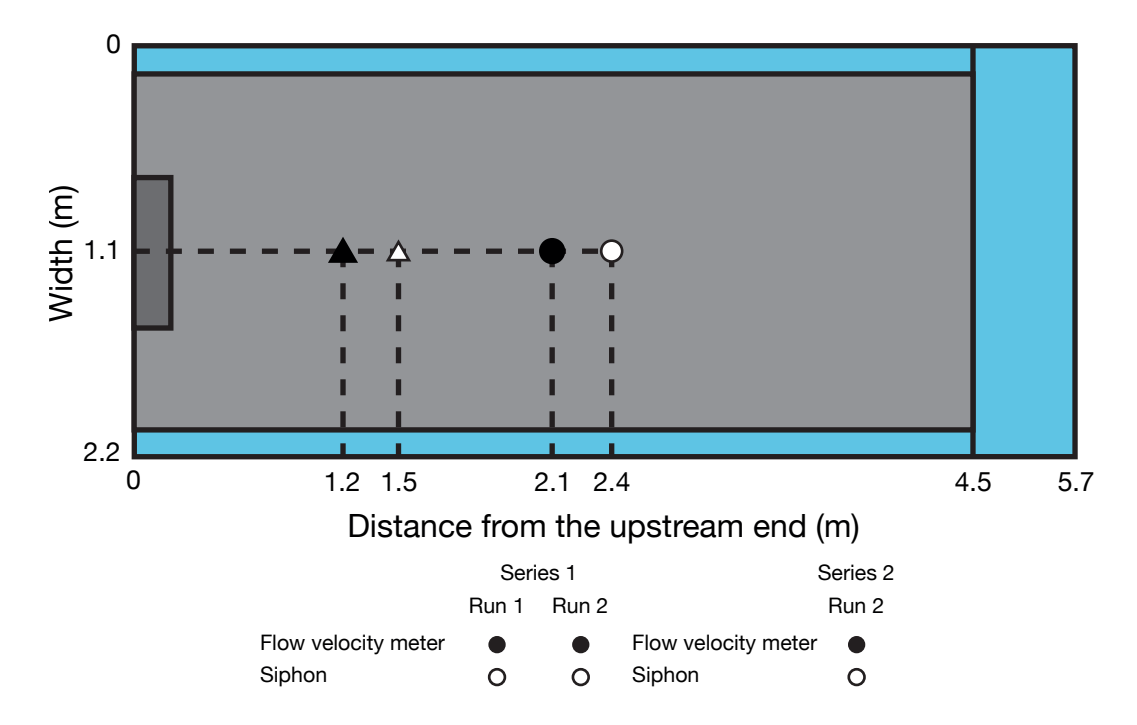


Figure 3. Measurement points of flow velocity and sampling points of suspended sediment in Series 1 and Series 2 performed in this study.

To measure suspended sediment concentrations, suspensions were sampled using 10 siphon tubes spaced every 0.01 m, ranging from 0.01 m to 0.1 m from the bottom. The sampling interval of the suspended sediment was constant in all experiments. The suspension was sampled at the center of the flume in the width direction. In the longitudinal direction, it was sampled at 2.4 m and 1.5 m from the upstream end for Series 1 and 2, respectively (Figure 3).

The sampled water and suspended sediment mixtures were accumulated in 300 mL beakers and weighed immediately after each run. In Series 1, the density of sampled water was measured using a digital density meter (DA-130N, Kyoto Electronics Manufacturing Co., Ltd.). The weights were measured again after drying to obtain the dried weight of suspended sediment. The grain size distributions of the accumulated sediment were measured using settling tubes with the open-source software Stube (Naruse, 2005).

The suspended sediment concentration for the ith grain size class was calculated from the measured values using the following equation:

$$c_i = \frac{\rho_f M_s F_{si}}{\rho_s M_w + \rho_f M_s},\tag{1}$$

where $M_{\rm w}$ and $M_{\rm s}$ denotes the mass of the fluid (saline or freshwater) and dried suspended sediment, respectively. F_{si} denotes the fraction of the *i*th grain-size class in the sampled suspended sediment. The $\rho_{\rm f}$ and $\rho_{\rm s}$ are the density of the fluid and sediment, respectively.

2.1.3 Data processing

212

213

215

216

217

218

219

220

222

223

225

226

227

228

230

231

232

233

234

235

237

238

239

240

241

242

243

In this study, the layer-averaged flow velocities and suspended sediment concentrations were calculated from the profiles measured by the ADVP and siphons during the experiment. The layer-averaged velocity U, flow height h, layer-averaged suspended sediment concentration of the *i*th grain size class C_i , and layer-averaged total suspended sediment concentration $C_{\rm T}$ were calculated using the following equations (Ellison & Turner, 1959):

$$Uh = \int_0^\infty u dz,\tag{2}$$

$$U^2 h = \int_0^\infty u^2 dz,\tag{3}$$

$$UC_i h = \int_0^\infty uc_i dz,\tag{4}$$

$$C_{\rm T} = \sum_{i} C_i,\tag{5}$$

where u and c_i denote the measured flow velocity and the suspended sediment concentration of the ith grain size class at the height z from the bed, respectively. To calculate Equations (2)-(4), the measured values were linearly interpolated to obtain the values at evenly spaced intervals. The flow velocity and suspended sediment concentration were extrapolated to obtain the values outside the measured regions using linear fitting to the two uppermost and lowermost measurement points.

In Run 1 of Series 1, the flow velocity could only be measured near the bed. For this run, the U, C_i , and h were calculated based on the following empirical relationship (Altinakar et al., 1996) using the values at the maximum velocity height:

$$\frac{U_{\text{max}}}{U} = 1.3,$$
 (6)
 $\frac{c_{\text{b}i}}{C_i} = 2,$ (7)
 $\frac{h_{\text{m}}}{h} = 0.3,$ (8)

$$\frac{c_{bi}}{C_i} = 2,\tag{7}$$

$$\frac{h_{\rm m}}{h} = 0.3,\tag{8}$$

where U_{max} denotes the maximum value in the vertical flow velocity profile, $c_{\text{b}i}$ denotes suspended sediment concentration of ith grain-size class at 0.05h, and $h_{\rm m}$ denotes the height from the bed that is U_{max} .

The layer-averaged density-equivalent sediment concentration for saline water $C_{\rm s}$ (hereafter the equivalent concentration) was defined as the particle concentration with zero settling velocity that would give the same excess density of the saline water. In Series 1, the density of siphon-sampled saline water was measured at suspended sediment sampling points (Figure 3). Assuming that the submerged specific density of particles $R = (-\rho_s/\rho_f - 1)$ is 0.49, the same as for the plastic particles, the density-equivalent sediment concentration $c_{\rm s}$ is calculated as follows:

$$c_{\rm s} = \frac{\rho_{\rm sw} - \rho_{\rm w}}{R\rho_{\rm w}},\tag{9}$$

where $\rho_{\rm w}$ and $\rho_{\rm sw}$ denote densities of fresh water and saline water, respectively. In this study, the density of fresh water was set to 1000 kg/m³. Subsequently, the layer-averaged equivalent sediment concentration (C_s) was calculated by applying Equation (4) to c_s .

2.1.4 Calculations of dimensionless parameters

The densimetric Froude, Reynolds, particle Reynolds, Shields, and critical Shields numbers were calculated from the hydraulic parameters averaged over the layers. The densimetric Froude number, Fr_d , is defined as follows:

$$Fr_{\rm d} = \frac{U}{\sqrt{\frac{\rho_{\rm t} - \rho_{\rm w}}{\rho_{\rm w}}gh}},\tag{10}$$

where $\rho_{\rm t}$ is the density of a turbidity current. The turbidity current density $\rho_{\rm t}$ can be obtained from:

$$\rho_{\rm t} = \rho_{\rm s} C_{\rm T} + \rho_{\rm sw} (1 - C_{\rm T}). \tag{11}$$

The parameter g is the gravity acceleration.

The Reynolds number was calculated using the following equation:

$$Re = \frac{Uh}{\nu}. (12)$$

Here, ν denotes the kinematic viscosity of water. Judging from the measured water temperature, the values of this variable were estimated to be 1.099×10^{-6} , 1.144×10^{-6} , and 0.896×10^{-6} for Run 1 and Run 2 of Series 1, and in Series 2, respectively (Nezu, 2019). The water temperature in Spychala et al. (2020) was not provided in their study; therefore, the kinematic viscosity of water at $20\,^{\circ}$ C, 1.002×10^{-6} , was used to calculate the Reynolds number (Nezu, 2019).

The Shields number τ_i^* was calculated using the following equation:

$$\tau_i^* = \frac{u_*^2}{RgD_{si}},\tag{13}$$

where

245

246

247

250

251

252

253

254

257

258

259

260

261

262

263

265

267

268

269

270

$$u_* = \sqrt{c_{\rm f}}U. \tag{14}$$

Here, where D_{si} exhibits the grain diameter of sediment particles of the *i*th grain-size class. The parameter c_f is the basal friction coefficient, which was calculated using the following equation:

$$c_{\rm f} = \left[\frac{1}{\kappa} \ln \left(11 \frac{h}{k_s} \right) \right]^{-2},\tag{15}$$

where κ denotes the Karman constant, which was set to 0.4. The roughness height of the bed k_s was calculated by $k_s = 2D_{s50}$ using mean grain-size D_{s50} .

The critical Shields number τ_{ci}^* was calculated using the following empirical relationship (Parker et al., 2003):

$$\tau_{ci}^* = \frac{1}{2} \left(0.22 Re_{pi}^{-0.6} + 0.06 \times 10^{-7.7 Re_{pi}^{-0.6}} \right), \tag{16}$$

where Re_{pi} is a particle Reynolds number, which is defined as follows:

$$Re_{\mathrm{p}i} = \frac{u_* D_{\mathrm{s}i}}{\nu}.\tag{17}$$

2.1.5 Topography and experimental deposits

Photographs of the experimental topographies were taken before and after the run, and digital elevation models (DEMs) of the experimental topographies were generated

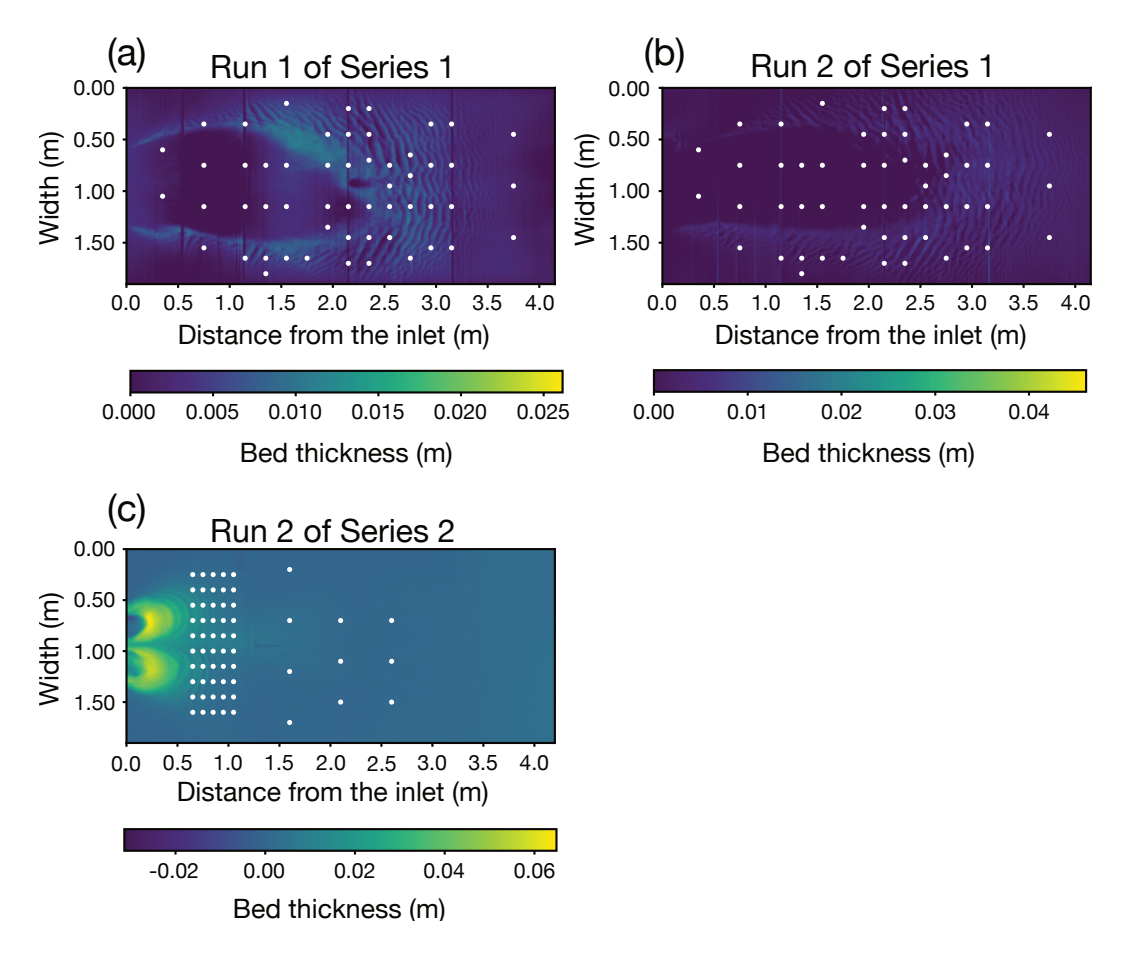


Figure 4. Sampling points of deposits in Series 1 and 2 conducted in this study. The white circles indicate the sampling points. (a) Sampling points in Run 1 of Series 1. (b) Sampling points in Run 2 of Series 1. (c) Sampling points in Run 2 of Series 2.

from these images (see details in Appendix A). The bed thickness η_T was then measured from the difference in elevation between the topography before and after each run.

After the topography was photographed, the experimental deposits were sampled from the flume floor, where water was drained using a drainage pump. The sampling intervals were changed according to the distribution of bed thickness of the experimental deposits. Dense sampling was performed in areas where bed thickness changed rapidly, and samples were collected at sparse intervals in areas where bed thickness gradually changed. We collected 54 samples from the experimental deposit of Series 1 at approximately equal intervals (Figures 4a, 4b). The sampling interval was approximately 10 cm in the longitudinal direction and 40–50 cm in the lateral direction. From the experimental deposit of Series 2, we collected 60 samples (Figure 4c). The sampling density was approximately 10 cm intervals in the upstream region, whereas it ranged from approximately 40 to 100 cm intervals in the downstream region.

The sediment volume (including porosity) per unit area of *i*th grain-size class η_i was then calculated at sampling points using the following equation:

$$\eta_i = V_{si}\eta_{\rm T},\tag{18}$$

where $V_{\mathrm{s}i}$ and η_{T} represent the sediment volume fraction of the *i*th grain-size class and bed thickness, respectively.

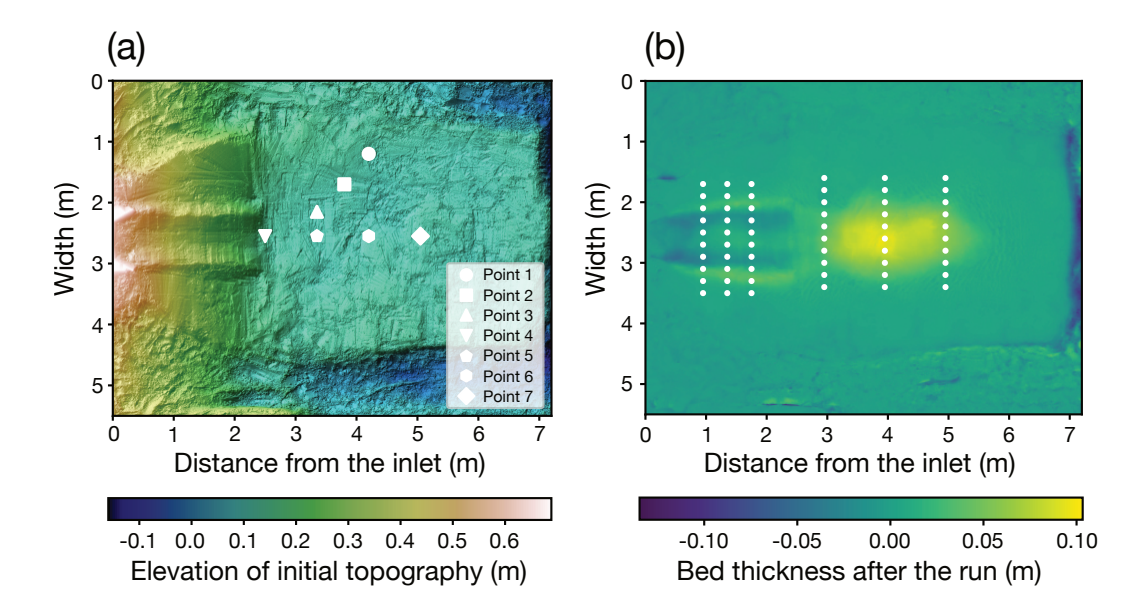


Figure 5. Measurement points of velocities and locations where bed thickness was extracted from bed thickness distribution datasets of Spychala et al. (2020). (a) Measurement points of flow velocities. (b) Locations at which bed thickness values were extracted from the distribution datasets provided by Spychala et al. (2020). The extracted bed thickness values were used as input for the inverse model.

2.2 Flume Experiment in Spychala et al. (2020)

The flume experimental dataset of Run 1 of Series 1 in the existing study (Spychala et al., 2020) was also used to verify the performance of the inverse model. The experiments in Spychala et al. (2020) were conducted in Eurotank at Utrecht University, which has a length of 11 m and a width of 6 m. Before the experiment, a channel was created in the upstream region as an initial topography. The water and sediment particles were mixed in the mixing tank before being released into the flume. The median grain size of the sediment particles used in this experiment was $133\,\mu\text{m}$, and the suspended sediment concentration in the mixing tank was set to 17%. A turbidity current flowed into the flume with a constant flow discharge of $30\,\text{m}^3/\text{s}$ for 80--100 seconds. During the experiment, flow velocities were measured at 7 points using Ultrasonic Velocity Profilers (Figure 5a).

The experimental flow conditions and bed thickness were obtained from the literature (Spychala et al., 2020). The layer-averaged flow conditions were not described in Spychala et al. (2020); therefore, we calculated the layer-averaged values of the flow velocity and height from the maximum flow velocities and their measured heights using Equations (6) and (8). The suspended sediment concentration in the experimental flume was not measured in the experiment of Spychala et al. (2020). Thus, the layer-averaged suspended sediment concentration was not compared with the predictions in this study. The bed thickness was calculated from the difference between the DEMs of the experimental topography before and after the run, which were provided by Spychala et al. (2020). In this study, a total of 60 points were sampled from the bed thickness distribution obtained from the DEM and used as input for the inverse model (Figure 5b).

2.3 Forward Model

311

312

313

314

315

316

317

318

319

320

322

323

324

325

326

327

328

329

330

331

333

334

335

336

337

338

342

343

344

This section describes the forward model of turbidity currents used to generate the training datasets for the inverse models. A 2D horizontal shallow-water equation model considering suspended sediment transport of the mixed grain-size classes was used to calculate the sediment volume per unit area of a turbidite for each grain-size class under the given model input parameters.

2.3.1 Governing equations

The model employed in this study is based on the four-equation model of turbidity currents proposed by Parker et al. (1986), which considers the momentum, mass, and turbulent kinetic energy conservation of the flow.

The governing equations of the model are as follows (Naruse, 2020):

$$\frac{\partial h}{\partial t} + \frac{\partial Uh}{\partial x} + \frac{\partial Vh}{\partial y} = e_{\mathbf{w}} \sqrt{U^2 + V^2},\tag{19}$$

$$\frac{\partial C_i h}{\partial t} + \frac{\partial U C_i h}{\partial x} + \frac{\partial V C_i h}{\partial y} = w_{si} (F_i e_{si} - r_0 C_i), \tag{20}$$

$$\frac{\partial Uh}{\partial t} + \frac{\partial U^2h}{\partial x} + \frac{\partial UVh}{\partial y} = -\frac{1}{2}Rg\frac{\partial C_{\rm T}h^2}{\partial x} + RgC_{\rm T}h\frac{\partial \eta_T}{\partial x} - c_{\rm f}U\sqrt{U^2 + V^2} + \nu_{\rm t}\left(\frac{\partial^2 Uh}{\partial x^2} + \frac{\partial^2 Vh}{\partial y^2}\right), \tag{21}$$

$$\frac{\partial Vh}{\partial t} + \frac{\partial UVh}{\partial x} + \frac{\partial V^2h}{\partial y} = -\frac{1}{2}Rg\frac{\partial C_{\rm T}h^2}{\partial y} + RgC_{\rm T}h\frac{\partial \eta_T}{\partial y} - c_{\rm f}V\sqrt{U^2 + V^2} + \nu_{\rm t}\left(\frac{\partial^2 Uh}{\partial x^2} + \frac{\partial^2 Vh}{\partial y^2}\right), \tag{22}$$

$$\frac{\partial Kh}{\partial t} + \frac{\partial UKh}{\partial x} + \frac{\partial VKh}{\partial y} = \left(c_{\rm f} + \frac{1}{2}e_{\rm w}\right)U^3 - \epsilon_0 h - Rgw_{\rm s}iC_{\rm T}h
- \frac{1}{2}RgC_{\rm T}hUe_{\rm w} - \frac{1}{2}Rghw_{\rm s}i(e_{\rm s}i - r_0C_{\rm T}),$$
(23)

where x and y are the horizontal bed-attached Cartesian coordinates, respectively, and t represents time. The parameter h denotes the flow height. C_i and C_T are the suspended sediment concentration of ith grain-size class and the total sediment concentration, respectively. The density-equivalent sediment concentration for saline water $C_{\rm s}$ was regarded as one of these concentrations in this study. The parameters U and V denote the layeraveraged flow velocities in the x and y directions, respectively. The layer-averaged turbulent kinetic energy is represented by K. The parameter η_T denotes the bed thickness. The volume fraction of the ith grain-size class in the active layer is denoted as F_i , and the dimensionless entrainment rates of the ambient fluid and basal sediment of ith grainsize class are expressed by $e_{\rm w}$, $e_{\rm si}$, respectively. The parameter $w_{\rm si}$ denotes the settling velocity of ith grain-size of a sediment particle of the ith grain-size class. The gravity acceleration g was set to $9.81 \,\mathrm{m/s^2}$ in this study. The parameter $c_{\rm f}$ denotes the friction coefficient, which was set at 0.004 and $\nu_{\rm t}$ denotes the horizontal eddy viscosity. The parameter r_0 is the ratio of the near-bed concentration to the layer-averaged concentration, which was set to 2.0 in this study. The dissipation rate of the layer-averaged turbulent kinetic energy K is denoted as ϵ_0 . Equation (19) represents the fluid mass conservation, and Equation (20) represents suspended sediment mass conservation. Equations (21) and (22) exhibit the flow momentum conservation in x and y directions. Equation (23) exhibits turbulent kinetic energy conservation.

The settling and entrainment fluxes of the sediment of the ith grain size class are calculated by the following equation:

$$\frac{\partial \eta_i}{\partial t} = \frac{w_{\rm si} \left(r_0 C_i - F_i e_{\rm si} \right)}{1 - \lambda_{\rm p}},\tag{24}$$

where η_i is the sediment volume per unit area of the *i*th grain-size class, λ_p denotes the porosity of the bed, which was set to 0.4 in this study. Thus, the temporal change in the total bed thickness η_T (i.e., deposition and erosion) is given by the Exner equation, which takes the following form:

$$\frac{\partial \eta_{\rm T}}{\partial t} = \sum \frac{\partial \eta_i}{\partial t}.$$
 (25)

The grain-size fraction F_i of the bed surface (i.e., the active layer) is required to calculate Equation (24). Assuming that the thickness of the active layer L_a is constant, the following equation denoting the mass conservation of the *i*th grain-size class in the active layer was used to obtain the temporal variation of the grain-size fraction F_i (Hirano, 1971; Cai & Naruse, 2021; Naruse & Nakao, 2021):

$$\frac{\partial F_i}{\partial t} + \frac{F_i}{L_a} \frac{\partial \eta_T}{\partial t} = \frac{w_{si}}{L_a (1 - \lambda_p)} \left(r_0 C_i - F_i e_{si} \right). \tag{26}$$

In this study, $L_{\rm a}$ was set to $0.003\,\mathrm{m}$ (Cai & Naruse, 2021; Cai, 2022).

2.3.2 Closure Equations

The following equations were employed to close the governing equations.

The friction velocity u_* was assumed to be related to the turbulent kinetic energy K following Parker et al. (1986). This assumption leads to the following relationship (Parker et al., 1986):

$$u_*^2 = \alpha K. \tag{27}$$

Here, the coefficient α was set to 0.6 in this study (Salinas et al., 2019).

The mean dissipation rate of the layer-averaged turbulent kinetic energy ϵ_0 is given by the following:

$$\epsilon_0 = \beta \frac{K^{1.5}}{h},\tag{28}$$

where

346

347

348

349

350

351

352

353

354

356

357

358

359

360

363

364

368

370

372

373

374

$$\beta = \frac{\alpha^{1.5}}{\sqrt{c_{\rm f}}}.\tag{29}$$

The eddy viscosity ν_t for the horizontal diffusion term of the momentum is calculated by the following empirical formulation:

$$\nu_{\rm t} = \frac{1}{6} \kappa u_* h. \tag{30}$$

Here, κ denotes the Karman constant, which is set to 0.4.

The settling velocity of *i*th grain-size class w_{si} was calculated by the equation of Ferguson and Church (2004):

$$w_{si} = \frac{RgD_{si}^2}{X_1\nu + (0.75X_2RgD_{si}^3)^{0.5}}. (31)$$

The kinematic viscosity of water ν was set to 1.099×10^{-6} was used in Run 1 of Series 1, 1.144×10^{-6} in Run 2 in Series 1, 0.896×10^{-6} in Series 2, and 1.002×10^{-6} in Spychala et al. (2020) as in 2.1.4. The empirical coefficients X_1 and X_2 are 18.0 and 1.0, respectively.

The empirical formulation of the entrainment rate of ambient fluid $e_{\rm w}$ takes the form (Parker et al., 1987):

$$e_{\rm w} = \frac{0.075}{\sqrt{1 + 718R_i^{2.4}}},\tag{32}$$

where R_i denotes the bulk Richardson number, which is defined as:

$$R_i = \frac{RgC_{\rm T}h}{U^2}. (33)$$

To obtain the basal sediment entrainment rate of the *i*th grain-size class e_{si} , the following empirical relationship was employed in this study (Kostic & Parker, 2006),

$$e_{\rm si} = \frac{aZ^5}{1 + \frac{a}{0.3}Z^5},\tag{34}$$

$$Z = \alpha_1 \frac{u_*}{w_{si}} Re_{pi}^{\alpha_2}, \tag{35}$$

$$(\alpha_1, \alpha_2) = \begin{cases} (0.586, 1.23) & Re_{pi} \le 2.36\\ (1.0, 0.6) & Re_{pi} > 2.36 \end{cases}, \tag{36}$$

where $a = 1.3 \times 10^{-7}$. Re_{pi} denotes the particle Reynolds number which is defined as

$$Re_{\mathrm{p}i} = \frac{\sqrt{RgD_{\mathrm{s}i}}D_{\mathrm{s}i}}{\nu}.\tag{37}$$

The computation of the model described above was implemented as the open-source software turb2d (Naruse, 2020). The turb2d employs the CIP-CUP method for the numerical scheme (Yabe & Wang, 1991), which solves the advection and pressure terms by the CIP and the implicit scheme, respectively. The artificial viscosity was used to stabilize the numerical results (Jameson et al., 1981; Ogata & Yabe, 1999). The wet-dry boundary condition was solved by the scheme of Yang et al. (2016).

2.4 Sensitivity Tests of the Forward Model against Input Model Parameters

To check the effect of the input model parameters on the depositional features, a sensitivity test was conducted. Case 1 was set as the standard case, and the cases were created in which $C_{0,i}$ (Case 2), U_0 (Case 6), h_0 (Case 7), and T_d (Case 8) of Case 1 were doubled, respectively (Table 2). In terms of $C_{0,s}$, Cases 3, 4, and 5 used values that were two, four and eight times greater than that of Case 1, respectively. The other conditions were the same as those of Run 1 of Series 1 in this study.

2.5 Inverse Model

In this study, deep neural networks (DNNs) were used to perform inverse analyses to estimate the flow conditions (i.e., model parameters) from the depositional features. These DNNs were trained using datasets generated by the forward calculations. After the training, the inverse model performances were tested using the test datasets produced independently from the training datasets. These processes are described in detail below.

2.5.1 Generation of Training Datasets

The training datasets for training the inverse models were generated by the forward model calculations. The size of the calculation domain and topographic setting were the same as those of the experimental tank used in Series 1 and 2 in this study and Run 1 of Series 1 in Spychala et al. (2020).

Table 2. Input parameters of forward model used in sensitivity test.

	Case 1	Case 2	Case 3	Case 4	Case 5	Case 6	Case 7	Case 8
$C_{0,1}$	0.001	0.002	0.001	0.001	0.001	0.001	0.001	0.001
$C_{0,2}$	0.001	0.002	0.001	0.001	0.001	0.001	0.001	0.001
$C_{0,3}$	0.001	0.002	0.001	0.001	0.001	0.001	0.001	0.001
$C_{0,4}$	0.001	0.002	0.001	0.001	0.001	0.001	0.001	0.001
$C_{0,\mathrm{s}}$	0.001	0.001	0.002	0.004	0.008	0.001	0.001	0.001
$U_0 (\mathrm{m/s})$	0.1	0.1	0.1	0.1	0.1	0.2	0.1	0.1
$h_0\left(\mathrm{m}\right)$	0.1	0.1	0.1	0.1	0.1	0.1	0.2	0.1
$T_{\rm d}$ (s)	100	100	100	100	100	100	100	200

The size of the calculation domain for experimental Series 1 and 2 was set to 4.2 m in length and 1.9 m in width, with a grid spacing of 0.05 m. The experimental flume was 4.5 m long, but 0.3 m from the upstream end was an inlet area, so the region was excluded from the calculation domain. In Run 1, the flat setting with 10% slope from the upstream end to 1.2 m and 5% from 1.2 m to the downstream end was set as the initial topography. The topography measured after the end of Run 1 of Series 1 was used as the initial topographic setting for Run 2 of Series 1. Similarly, the topography measured after the end of Run 1 of Series 2 was used for Run 2 of Series 2. The representative diameters of the four grain-size classes 1–4 of suspended sediment were set to be 210 μ m, 149 μ m, 105 μ m, and 74.3 μ m for both Series 1 and Series 2, respectively. The parameters C_1 , C_2 , C_3 , and C_4 denote the suspended sediment concentration for these grain-size classes.

To generate the training datasets for Run 1 of Series 1 in the existing study (Spychala et al., 2020), we used the initial topography obtained from a DEM measured before the experiment. The calculation domain had a length of 7.2 m from the inlet and a width of 1.9 m. The representative diameter of the suspended sediment was the same as the median diameter of the sediment particles used in the experiment, which was $133\,\mu\mathrm{m}$.

Thus, the upstream boundary conditions of the calculation domain were the Dirichlet boundary condition, where the flow height h_0 , the flow velocity U_0 , the suspended sediment concentration of ith grain-size class $C_{0,i}$, and the equivalent salt concentration $C_{0,s}$ were set to be fixed values. The inflow conditions at the upstream end were kept constant for $T_{\rm d}$ seconds in the forward model calculation. As described above, salt water was not used in Series 2 performed in this study and Run 1 of Series 1 in Spychala et al. (2020) so that the value of $C_{0,s}$ was zero in the calculation domain for these Series. The flow inlet was set to be 0.64 m in width at the upstream end in the experiments performed in this study and 0.45 m in Series in Spychala et al. (2020). Neumann boundary conditions were used for the right, left, and downstream boundaries, where the gradients of all variables were set to zero. In summary, the forward model requires the following input parameters: h_0 , U_0 , $C_{0,i}$, $C_{0,s}$ (only for Series 1 performed in this study), and $T_{\rm d}$. These parameters were subjected to the inverse analysis.

The training, validation, and test datasets for the inverse model were generated through iterations of the forward model calculation. The model input parameters described above were randomly generated from a uniform distribution with the prescribed ranges (Table 3), and the forward model calculation was repeated to produce the datasets of the sediment volume per unit area according to the given input parameters. The combined datasets of the calculated deposits and the model input parameters were split into training, validation, and test datasets, which were used to train and test the inverse model. In this study, the inverse models were trained using 10000 training datasets. During train-

ing, 20% of the training datasets were used as validation datasets. The performances of the inverse models were evaluated using 100 artificial test datasets generated independently of the training and validation datasets.

Table 3. Range of model input parameters at the inlet to generate training datasets.

	Series 1		Ser	Series 2		Spychala et al. (2020)	
	Min value	Max value	Min value	Max value	Min value	Max value	
$C_{0,i}$	0.0001	0.005	0.0001	0.005	0.01	0.15	
$C_{0,\mathrm{s}}$	0.001	0.03	-	-	-	-	
$U_0(\mathrm{m/s})$	0.005	0.5	0.005	0.5	0.1	2.0	
h_0 (m)	0.01	0.5	0.01	0.5	0.01	0.5	
$T_{\rm d}$ (s)	30	400	30	400	30	200	

2.5.2 Training of Deep Neural Networks

446

447

448

449

452

453

455

456

457

459

460

461

463

This study employed DNNs as inverse models (Figure 6). A fully connected (dense) neural network was adopted as the network structure. The inputs of the DNN were the thickness and grain-size distributions of the turbidites deposited in the calculation domain. Thus, the input values for the neural network were the volumes per unit area of four grain-size classes at the sampling points, and the network outputs the estimated input parameters of the forward model, including the flow height, flow velocity, sediment concentration for each grain size class, equivalent concentration, and flow duration. The equivalent concetration was excluded as the subject of inversion for Series 2 because it was conducted without salt water. The number of hidden layers and number of nodes per hidden layer were set to 4 and 4000, respectively. Rectified Linear Unit (ReLU) was employed as an activation function for the hidden layers for Series 1 and Series 2 conducted in this study (Nair & Hinton, 2010), In the run in Spychala et al. (2020), the sediment volume per unit area could be negative because the velocity of the current was very fast, and the current could erode the bed sediment. Therefore, when the input is negative, the use of ReLU may lead to vanishing gradients. Thus, Exponential Linear Unit (eLU) (Clevert et al., 2016), which produces non-zero outputs even for negative inputs, was used as an activation function for the hidden layer. The activation function in the output layer was ReLU in all experiment. These neural networks were implemented using Python 3.7 and TensorFlow 2.4.1.

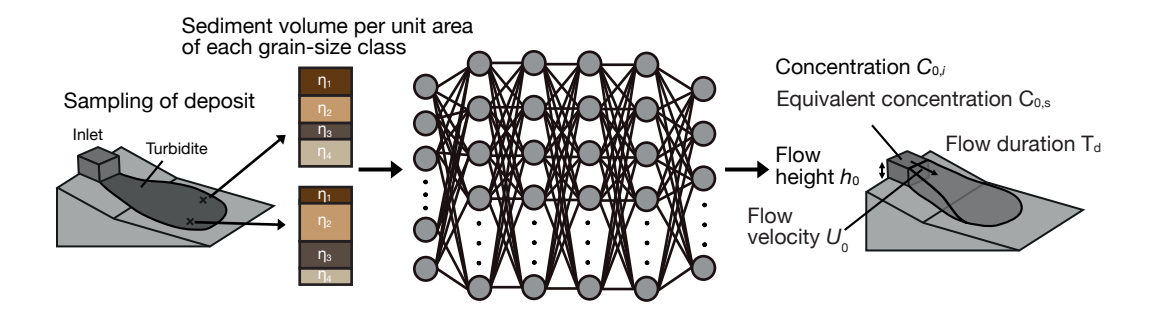


Figure 6. Schematic diagram of the inverse model structure. The inverse model takes as input the sediment volumes per unit area for each grain-size class at the sampling points. The outputs are the estimated model input parameters.

The training conditions were as follows. All hyperparameters for training were determined by trial and error. The Mean Squared Error (MSE) was employed as a loss function, and Adagrad was used as the optimizer of weight coefficients (Duchi et al., 2011). To prevent overlearning, the dropout method was employed (Srivastava et al., 2014), which deactivates 50% of the nodes randomly during training for Series 1 and Series 2 performed in this study, and 30% of the nodes deactivates for Spychala et al. (2020). The batch size and learning rate were set to 64 and 0.032, respectively. Under these conditions, the DNNs were trained for 10,000 epochs.

2.5.3 Test of Inverse Models

The inverse models were tested using 100 test datasets generated independently of the training datasets. The root mean squared error (RMSE), the bias (b) and symmetric mean absolute percentage error (SMAPE) were calculated for each model input parameter to evaluate the inverse model predictions. The RMSE, b, and SMAPE were defined as follows:

$$RMSE = \sqrt{\frac{1}{N} \sum_{i} (y_{pi} - y_i)^2}, \qquad (38)$$

$$b = \frac{1}{N} \sum_{i} (y_{pi} - y_i), \qquad (39)$$

$$SMAPE = \frac{100}{N} \sum_{i} \frac{2|y_i - y_{pi}|}{|y_i| + |y_{pi}|},$$
(40)

where N denotes the number of test datasets. The variables y_i and y_{pi} denote true and model-predicted values, respectively.

2.6 Inversion of experimental deposits

The inverse models developed in this study were applied to the experimental deposits to evaluate the performance of the inverse model for actual turbidity currents and reconstruct the experimental flow conditions and horizontal two-dimensional distribution of deposits. Inverse analyses were performed on three experimental deposits formed by experiments in this study (Runs 1 and 2 of Series 1 and Run 2 of Series 2) and one deposit formed in Spychala et al. (2020) by inputting the sediment volume per unit area of each grain-size class at the sampling points.

To obtain the flow conditions at the measurement point, forward calculations were performed using the model input parameters estimated by the inverse models. The estimated layer-averaged flow velocities, suspended sediment concentrations, flow heights, and flow durations were compared with the measured values to verify the performance of the inverse models. The verification of inverse models was based on the SMAPE and normalized percentage error (NPE). The NPE was calculated using the following equation:

$$NPE = 100 \times \frac{2|y_{\rm m} - y_{\rm p}|}{|y_{\rm m}| + |y_{\rm p}|}.$$
 (41)

Here, $y_{\rm m}$ and $y_{\rm p}$ denote the measured and predicted values, respectively. Regarding the flow duration $T_{\rm d}$ reported by Spychala et al. (2020), which ranged from 80 to 100 seconds, the SMAPE and NPE were calculated using both the minimum and maximum values.

The distributions of bed thickness obtained from numerical calculations using the predicted model input parameters were compared with the measured bed thickness. In this study, the calculations were conducted with a grid spacing of 0.05 m, so variations

of bed thickness with wavelengths smaller than this could not be reproduced. Accordingly, the comparisons between the predicted and measured bed thickness were performed at 0.05 m intervals.

3 Results

3.1 Experimental flow behaviors and topographic features

The experimental turbidity currents flowed downstream from the inlet and laterally spread. The heights of the currents increased as they flowed downstream due to the entrainment of ambient fluid. The turbidity current reached the downstream end at 23 and 28 seconds after the initiation of the flow injection in Runs 1 and 2 of Series 1. On the other hand, it took 180 seconds for the flow to reach the downstream end in Run 2 of Series 2. Each flow was maintained at a constant flow discharge for a specified period, and no significant changes in the flow behaviors were observed during the experiments after they reached the downstream end.

The topographies developed from the experimental turbidity currents differed significantly between experimental Series 1 and 2. In Series 1, a channel-levee-like topography was developed, where the erosional depression was located near the flow inlet, and lobate deposits were formed in the downstream area. In contrast, the topography in Series 2 was smooth and exhibited no depressions around the flow inlet. In all runs, it was difficult to distinguish the influence of those topographies on the flow behavior with the naked eye. The ripples were observed in the experimental deposits in all runs. In Run 1 and Run 2 of Series 1, the ripples were formed on the lobe deposits in the downstream area, whereas they were observed in the upstream area near the flow inlet in Series 2.

3.2 Measured profiles of experimental turbidity currents

In all velocity profiles at the measured point (Figure 3), the flow velocities increased upward above the bottom surface, and after it reached the maximum velocity, the velocities subsequently decreased upward gradually (Figures 7a, 7c, 7e). The maximum flow velocities were observed at a height of 0.06 m in Run 1 of Series 1 and 0.0405 m above the bed in Series 1, while they were observed at a height of 0.0201 m above the bed in Series 2 (Figures 7a, 7c, 7e). The maximum velocity in Run 1 and Run 2 of Series 1 were 0.288 m/s and 0.393 m/s, respectively. In Run 1 of Series 2, the flow velocity was lower than that of Series 1, which was 0.0902 m/s.

The layer-averaged flow velocity U was estimated from the measured velocity profiles, which were 0.222 m/s in Run 1 of Series 1 and 0.254 m/s in Run 2 of Series 1 (Table 4). The layer-averaged flow velocity in Run 2 of Series 2 was lower than in Series 1, which was 0.0506 m/s (Table 4). The flow heights h were also calculated as 0.2 m, 0.254 m, and 0.200 m in Runs 1 and 2 of Series 1 and Run 1 of Series 2, respectively (Table 4).

The suspended sediment concentration at the measured points in all runs exhibited an exponential decrease upward (Figures 7b, 7d, 7f). The maximum values of total suspended sediment concentration recorded at the lowest elevation (1 cm above the bed) in Runs 1 and 2 of Series 1 were 0.00482 and 0.00344, respectively. In Run 1 of Series 2, the maximum value of suspended sediment concentration was 0.00515.

The layer-averaged values of total suspended sediment concentrations $C_{\rm T}$ were the same order of magnitude in all experimental series (Table 4). The Runs 1 and 2 of Series 1 were 2.41×10^{-3} and 1.90×10^{-3} in the layer-averaged concentration, respectively. The layer-averaged total concentration was 1.38×10^{-3} in Run 1 of Series 2.

Focusing on the layer-averaged concentration by grain size, Runs of Series 1 showed that the concentration increased with larger grain size (Table 4). The layer-averaged con-

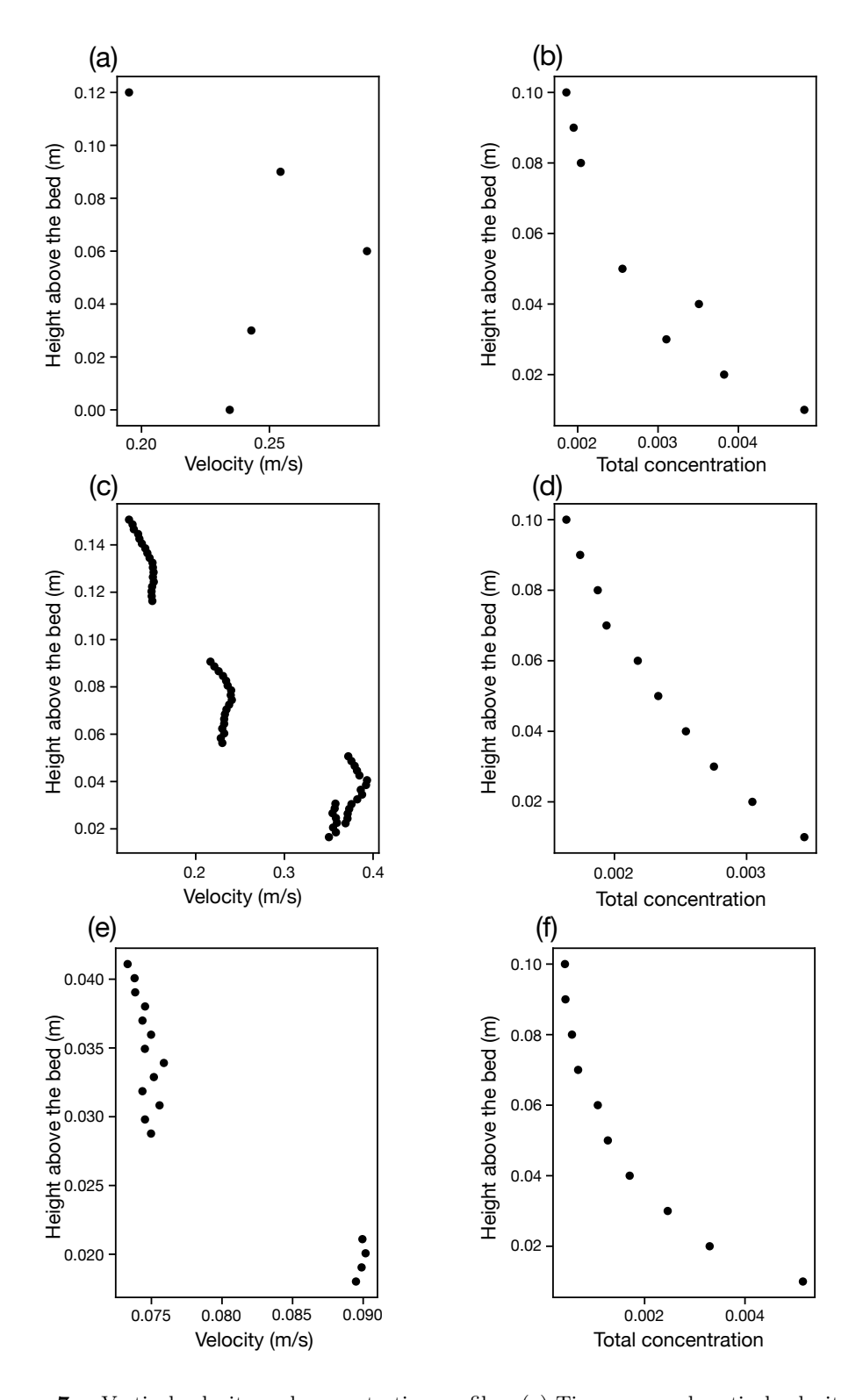


Figure 7. Vertical velocity and concentration profiles. (a) Time-averaged vertical velocity profile in Run 1 of Series 1. (b) Suspended sediment concentration profile in Run 1 Series 1. (c) Time-averaged vertical velocity profile in Run 2 of Series 1. (d) Suspended sediment concentration profile in Run 2 of Series 1. (e) Time-averaged vertical velocity profile in Run 2 of Series 2. (f) Suspended sediment concentration profile in Run 2 of Series 2.

Table 4. Layer-averaged flow conditions of flume experiments conducted in this study.

	Seri	Series 1		
	Run 1	Run 2	Run 2	
C_1	9.66×10^{-4}	5.71×10^{-4}	5.87×10^{-5}	
C_2	6.81×10^{-4}	4.65×10^{-4}	4.08×10^{-4}	
C_3	5.54×10^{-4}	4.78×10^{-4}	5.50×10^{-4}	
C_4	2.08×10^{-4}	3.87×10^{-4}	3.64×10^{-4}	
$C_{ m T}$	2.41×10^{-3}	1.90×10^{-3}	1.38×10^{-3}	
$C_{ m s}$	5.20×10^{-3}	7.43×10^{-3}	-	
$U\left(\mathrm{m/s}\right)$	0.222	0.254	0.00501	
$h\left(\mathbf{m}\right)$	0.2	0.168	0.420	

centration of the largest grain size class (210 µm) were 9.66×10^{-4} , while the layer-averaged concentration of smallest grain size class (74.3 µm) was 2.08×10^{-4} . In contrast, the concentrations of Series 2 showed no clear trend, with the layer-averaged values ranging from 5.87×10^{-5} for C_1 to 5.50×10^{-4} for C_3 .

3.3 Dimensionless parameters of the experimental flows

The calculated dimensionless parameters $Fr_{\rm d}$ and Re indicated that all experimental turbidity currents were fully turbulent and supercritical flows (Tables 5, 6). The densimetric Froude numbers $Fr_{\rm d}$ of Runs 1 and 2 of Series 1 conducted in this study were 3.13 and 3.68, respectively. Although these values were slightly larger than that of Series 2, which was 1.62, $Fr_{\rm d}$ of all runs were significantly larger than unity. In addition, the Reynolds numbers Re ranged from 2080 to 46400, indicating that all experimental turbidity currents in this study and Spychala et al. (2020) were fully turbulent.

The Shields numbers τ_i^* and particle Reynolds number Re_{pi} showed that the resuspension of the transported sediment hardly occurred at around the measurement points in the experiments conducted in this study (Table 5). The particle Reynolds numbers Re_{pi} were smaller than 5 in experimental runs in this study, indicating that these runs were performed under hydraulically smooth conditions (Garcia, 2008). The Shields numbers of ith grain-size classes τ_i^* in Series 1 ranged from 0.0465–0.132, which were slightly smaller than the threshold for motion (the critical Shields number τ_{ci}^*). In addition, the Shields numbers τ_i^* in Series 2 were significantly smaller than the critical Shields number

In the experiment in Spychala et al. (2020) whose datasets were utilized in this study, the resuspension of the bed sediment could occur in the area along the central line of the flow. The Shields number τ^* was larger than τ_c^* near the Points 4–7 which were near the center of the flume, while τ^* was smaller than τ_c^* Points 1–3 near the edge of flume (Figure 5a, Table 6). The particle Reynolds numbers Re_{pi} ranged from 0.628 to 4.43, indicating that the flow regime was hydraulically smooth, as was the case in the runs conducted in this study.

3.4 Influence of input model parameters on depositional features

The numerical experiments indicated that the input parameters $C_{0,i}$, U_0 , h_0 , and T_d significantly affect the depositional features of the experimental turbidity currents. Case 2 (two times greater than $C_{0,i}$ in Case 1) resulted in preferential deposition around the upstream region of the calculation domain, which was significantly thicker than that of Case 1 (standard case) (Figures 8a, 8b, 9). The flow velocity U_0 also largely affected

Table 5. Densimetric Froude number, Reynolds number, Particle Reynolds number, Shields number, and critical Shields number in the experiments.

	Seri	es 1	Series 2
	Run 1	Run 2	Run 2
$Fr_{\rm d}$	3.12	3.68	1.62
Re	40300	37500	13100
Re_{p1}	1.93	2.12	0.532
Re_{p2}	1.37	1.50	0.377
Re_{p3}	0.962	1.06	0.266
Re_{p4}	0.681	0.749	0.188
$ au_1^*$	0.0465	0.0424	0.00509
$ au_2^*$	0.0656	0.0598	0.00718
$ au_3^*$	0.0931	0.0849	0.0102
$ au_4^*$	0.132	0.120	0.0144
$ au_{c1}^*$	0.0742	0.0701	0.161
$ au_{c2}^*$	0.0912	0.0862	0.197
$ au_{c3}^*$	0.1125	0.106	0.244
$ au_{c4}^*$	0.138	0.131	0.300

Table 6. Reynolds number, particle Reynolds number, Shields number, and critical Shields number in the experiment in Spychala et al. (2020).

	Spychala et al. (2020)						
	Point 1	Ponit 2	Point 3	Point 4	Point 5	Point 6	Point 7
Re	2080	3940	16300	46400	20200	14000	9750
$Re_{\mathrm{p}} \\ \tau^*$	0.628	0.870	2.11	4.43	3.26	2.12	1.57
$ au^*$	0.0104	0.0200	0.118	0.517	0.280	0.118	0.0650
$ au_c^*$	0.145	0.120	0.0703	0.451	0.0541	0.0702	0.0839

the bed thickness. When U_0 was doubled (Case 6), the sediment was almost bypassed near the inlet, and the bed thickness was extremely thinner than that of Case 1 from the inlet to 0.9 m (Figures 8f, 9).

On the other hand, when the flow duration $T_{\rm d}$ was changed, the geometry of the deposits remained unchanged, but the overall thickness varied, which was clearly indicated in the result of Case 8 (Figures 8a, 8h, 9). The calculation result was slightly less sensitive to the flow height h_0 (Case 7) than other parameters, such as $C_{0,i}$, U_0 and $T_{\rm d}$. Nevertheless, the bed geometry distinctively differed from the base case (Case 1) when h_0 was doubled (Figures 8a, 8g, 9).

In contrast, the equivalent salt concentration $C_{0,s}$ did not significantly affect the turbidite bed geometry compared with the other input parameters (Figures 8c, 8d, 8e, 9). Even though the parameter $C_{0,s}$ increased twice or four times greater than that of Case 1, Cases 3 and 4 produced almost the same profiles of bed thickness as Case 1. Case 5, which set $C_{0,s}$ to eight times greater than that of Case 1, produced a slightly thinner deposit than that of Case 1, but the difference in bed thickness between Cases 1 and 5 was not significant.

3.5 Training and Tests of Inverse Models

The DNN models were sufficiently trained without significant overlearning (Figure 10). In the training histories of all DNN models, the validation loss decreased in tandem with the training loss. The value of the loss function decreased rapidly in the first 1000 epochs, and the learning curve became almost flat after 8000 epochs.

The DNN model predictions for the test datasets indicated that the developed inverse models precisely estimated the flow conditions, including the suspended sediment concentrations $C_{0,i}$, flow velocity U_0 , flow height h_0 , and flow duration $T_{\rm d}$ (Figures 11, 12, 13, 14; Tables 7, 8, 9). The flow height h_0 and flow duration $T_{\rm d}$ were reproduced with high accuracy, showing the range of SMAPE from 13.9% to 24.8% and from 18.5% to 23.6%, respectively (Figures 11g–11h, 12g–12h, 13f–13g, 14c–14d; Tables 7, 8, 9). Regarding the biases, the estimated flow duration was slightly underestimated in all runs. The suspended sediment concentrations $C_{0,i}$ were also estimated with small SMAPEs, ranging from 17.6% to 28.4% (Figures 11a–11d, 12a–11d, 13a–11d, 14a; Tables 7, 8, 9). The RMSEs and biases of $C_{0,i}$ ranged from 10^{-5} to 10^{-4} in Series 1 and Series 2 performed in the present study, and the RMSE and bias were 0.0134 and -0.00232, respectively, in Spychala et al. (2020) (Tables 7, 8, 9). The flow velocity U_0 was well estimated, with SMAPE values ranging from 15.0% to 32.5%, and RMSEs of U_0 were 0.0489 m/s or less (Figures 11f, 12f, 13e, 14b; Tables 7, 8, 9).

In contrast, estimating the equivalent concentration $C_{0,\rm s}$ was difficult compared with the other parameters (Figures 11e, 12e, Table 7). The SMAPE values of $C_{0,\rm s}$ in Run 1 and Run 2 of Series 1 were 71.2% and 66.0%, respectively. These corresponded to RM-SEs of 5.45×10^{-3} and 1.06×10^{-3} , respectively.

3.6 Experimental Verification of Inverse Models

The inverse models developed in this study estimated the flow conditions of experimental turbidity currents from deposits within reasonable ranges (Figure 15; Tables 10, 11, 12, 13). The SMAPE values showed that the layer-averaged flow velocities U were most accurately reproduced, with a SMAPE of 51.7% (Table 14). The flow heights h and flow durations $T_{\rm d}$ were also estimated with reasonable accuracy. The normalized percentage errors of h and $T_{\rm d}$ were 15.7%–90.4% and 38.5%–86.3%, respectively (Tables 11, 12, 13). The SMAPE of the suspended sediment concentrations of ith grain-size class C_i and the total suspended sediment concentration $C_{\rm T}$ were also estimated reasonably, but were slightly larger than those of the other flow conditions. In addition, the normal-

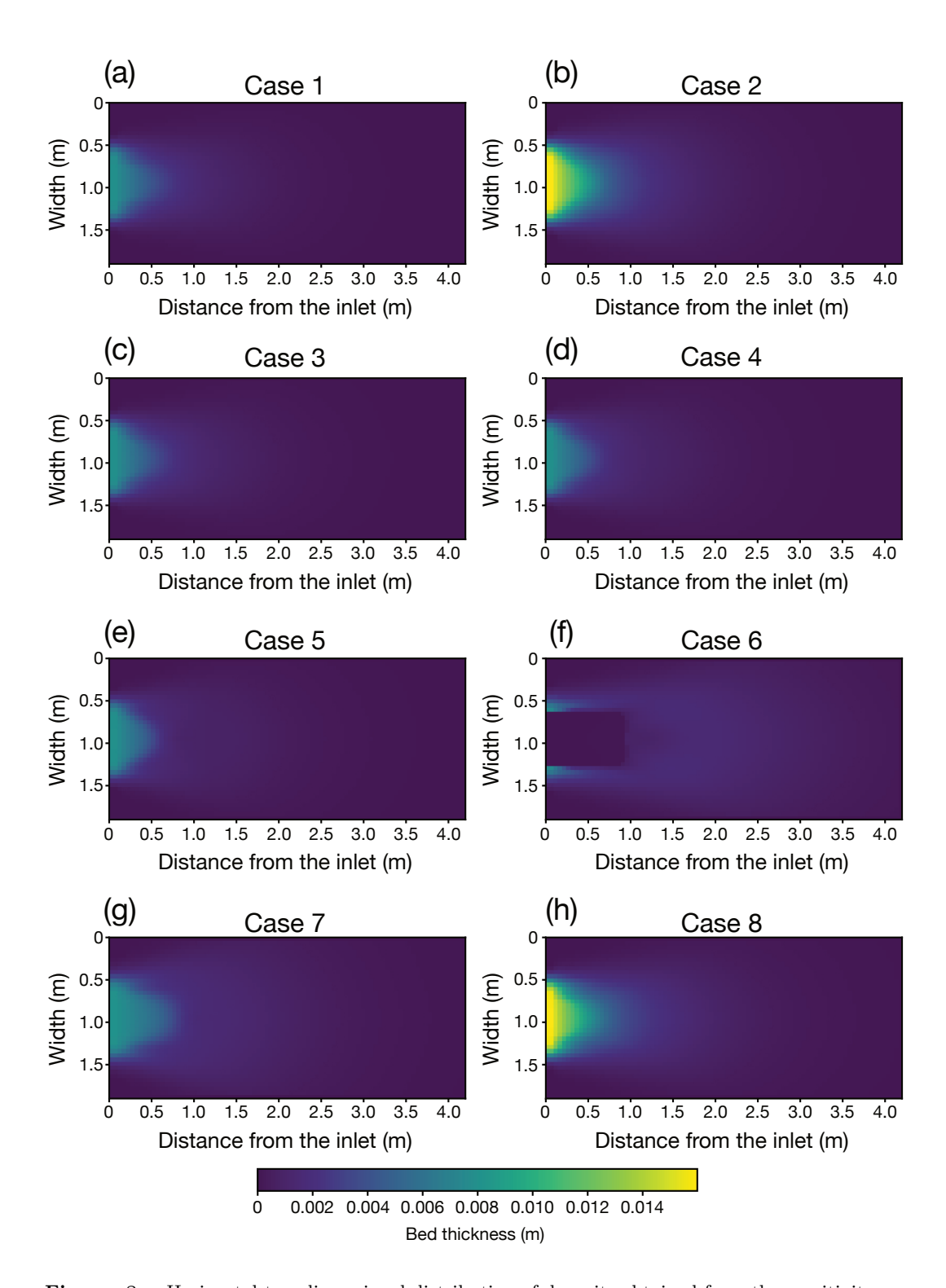


Figure 8. Horizontal two-dimensional distribution of deposits obtained from the sensitivity test. (a) Bed thickness of Case 1. (b) Bed thickness of Case 2. (c) Bed thickness of Case 3. (d) Bed thickness of Case 4. (e) Bed thickness of Case 5. (f) Bed thickness of Case 6. (g) Bed thickness of Case 7. (h) Bed thickness of Case 8.

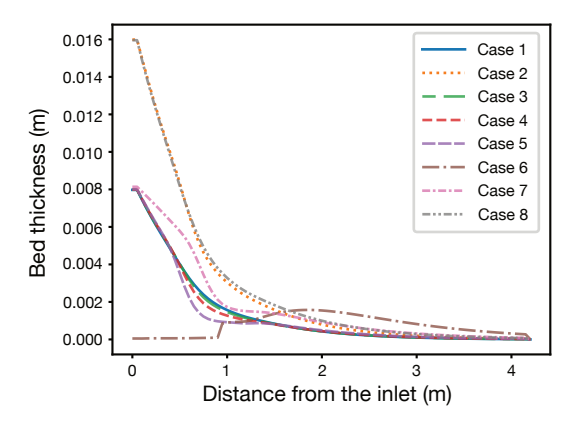


Figure 9. Comparison of bed thickness distributions under different input parameters. The bed thicknesses are compared along the longitudinal cross-section at the center of the flume.

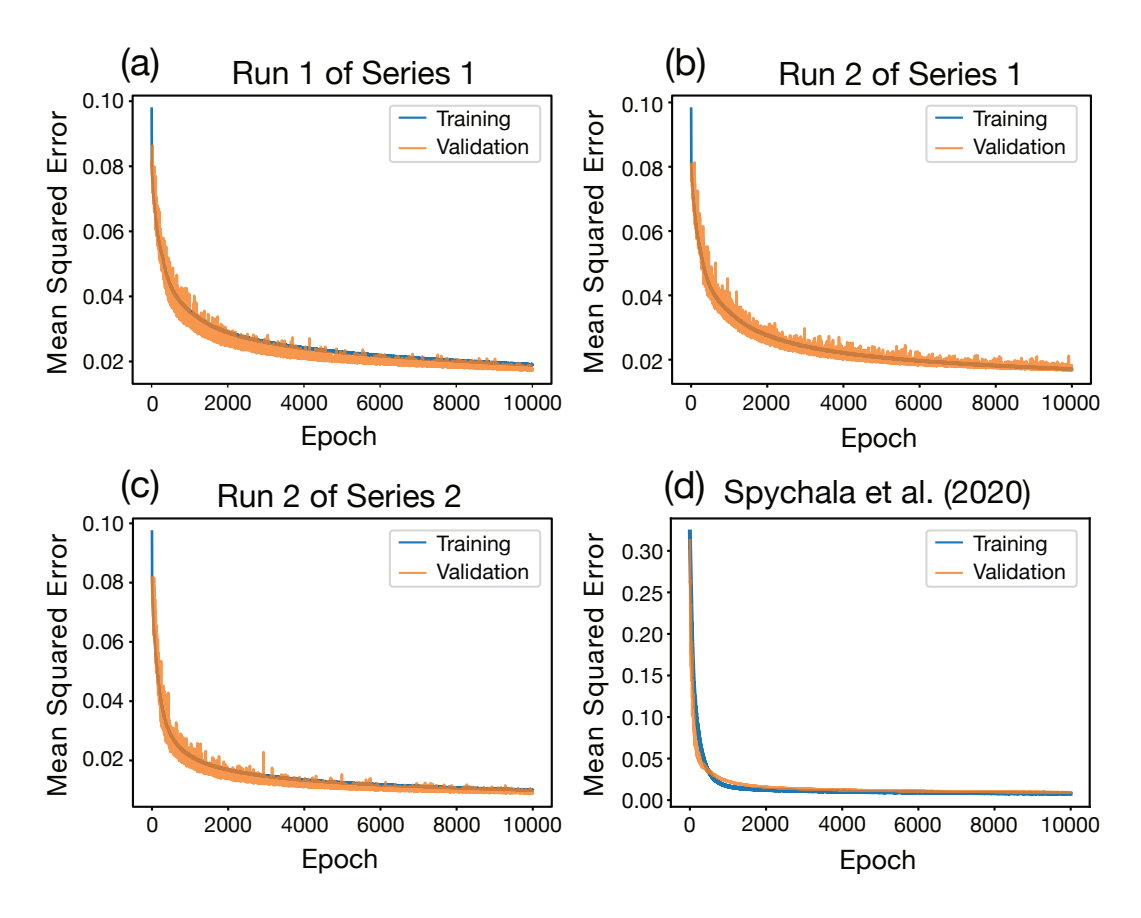


Figure 10. Training histories of the inverse models. (a) Training history of Run 1 of Series 1. (b) Training history of Run 2 of Series 1. (c) Training history of Run 2 of Series 2. (d) Training history of Spychala et al. (2020)

 $\textbf{Table 7.} \quad \text{RMSE, bias, and SMAPE of testing results of the inverse model for Series 1.}$

	Series 1							
	Run 1			Run 2				
	RMSE	Bias	SMAPE	RMSE	Bias	SMAPE		
$C_{0,1}$	7.34×10^{-4}	1.33×10^{-5}	28.2%	5.72×10^{-4}	4.37×10^{-5}	28.0%		
$C_{0,2}$	6.43×10^{-4}	-2.65×10^{-4}	28.0%	5.19×10^{-4}	7.97×10^{-5}	17.8%		
$C_{0,3}$	5.84×10^{-4}	-1.64×10^{-5}	19.1%	6.23×10^{-4}	1.12×10^{-4}	17.6%		
$C_{0,4}$	5.45×10^{-4}	-1.11×10^{-4}	26.1%	5.98×10^{-4}	-7.15×10^{-5}	22.0%		
$C_{0,\mathbf{s}}$	5.45×10^{-3}	-1.38×10^{-4}	71.2%	4.19×10^{-3}	1.06×10^{-3}	64.6%		
U_0	0.0443 m/s	-0.0123 m/s	32.5%	0.0489 m/s	$1.09 \times 10^{-4} \text{ m/s}$	26.0~%		
h_0	$0.0637~\mathrm{m}$	$0.0107~\mathrm{m}$	22.0%	$0.0528~\mathrm{m}$	-0.00579 m	24.8%		
$T_{ m d}$	$50.7 \mathrm{\ s}$	-20.3 s	23.6%	$40.0 \mathrm{\ s}$	-18.2 s	18.5%		

 $\textbf{Table 8.} \quad \text{RMSE, bias, and SMAPE of testing results of the inverse model for Series 2.}$

	Series 2			
		Run 2		
	RMSE	Bias	SMAPE	
$C_{0,1}$	4.90×10^{-4}	8.52×10^{-5}	18.0%	
$C_{0,2}$	4.11×10^{-4}	5.93×10^{-5}	19.5%	
$C_{0,3}$	5.60×10^{-4}	9.75×10^{-5}	19.1%	
$C_{0,4}$	5.19×10^{-4}	9.14×10^{-5}	28.4%	
U_0	$0.0383 \; \text{m/s}$	$3.16 \times 10^{-4} \text{ m/s}$	20.4%	
h_0	$0.0337~\mathrm{m}$	-0.00476 m	13.9%	
$T_{\rm d}$	51.1 s	-34.1 s	22.9%	

Table 9. RMSE, bias, and SMAPE of testing results of the inverse model for Run 1 of Series 1 in Spychala et al. (2020).

	Spy	Spychala et al. (2020)					
	RMSE	Bias	SMAPE				
$C_{0,1}$	0.0134	-0.00232	22.1%				
U_0	$0.123 \mathrm{\ m/s}$	-0.00315 m/s	15.0%				
h_0	$0.0266~\mathrm{m}$	$-0.00631 \mathrm{\ m}$	14.7%				
$T_{ m d}$	$20.3 \mathrm{\ s}$	-13.8 s	22.5%				

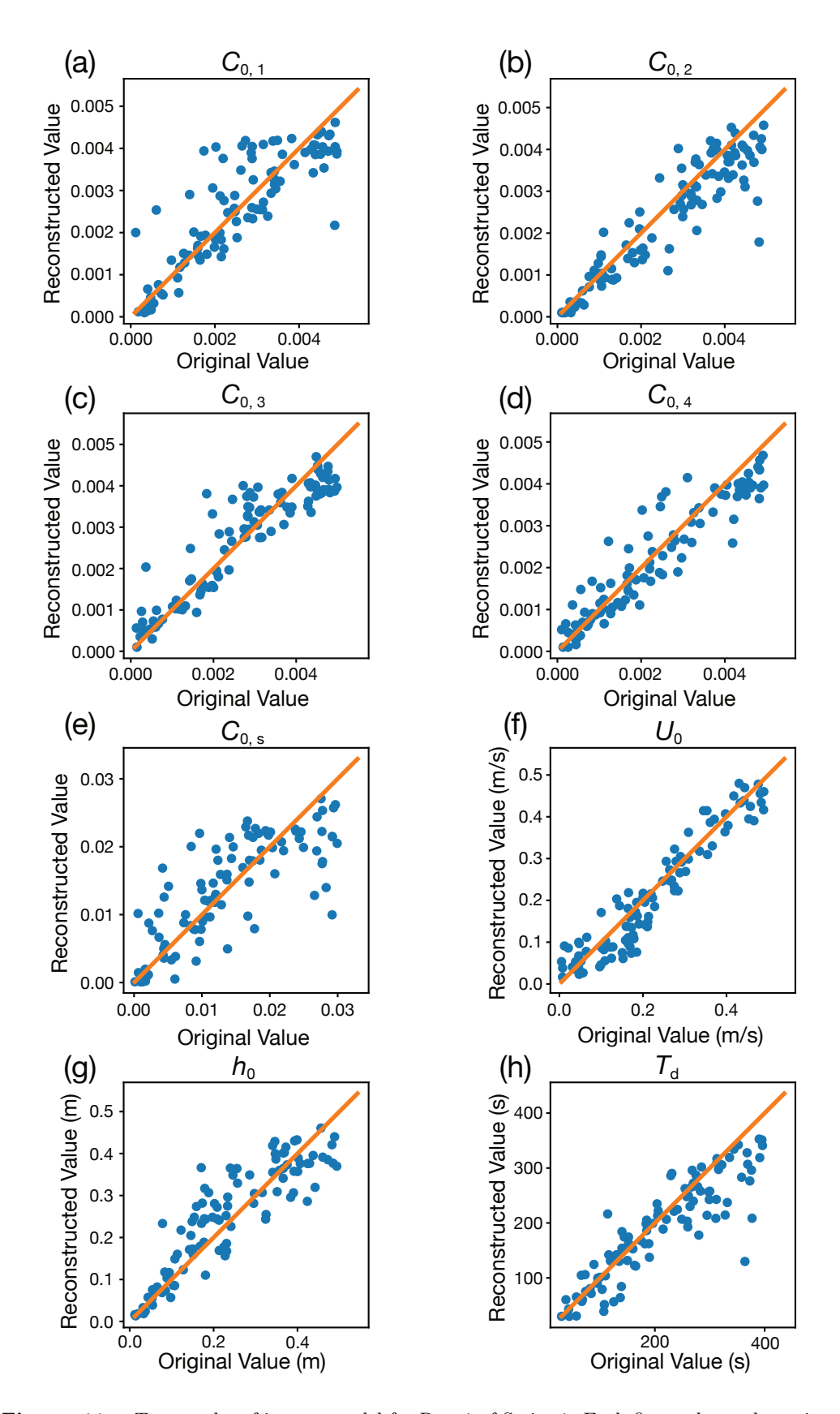


Figure 11. Test results of inverse model for Run 1 of Series 1. Each figure shows the estimation accuracy of the input parameters of the forward model. (a)–(d) Suspended sediment concentration of each grain-size class at the inlet. (e) Equivalent concentration at the inlet. (f) Flow velocity at the inlet. (g) Flow height at the inlet. (h) Flow duration.

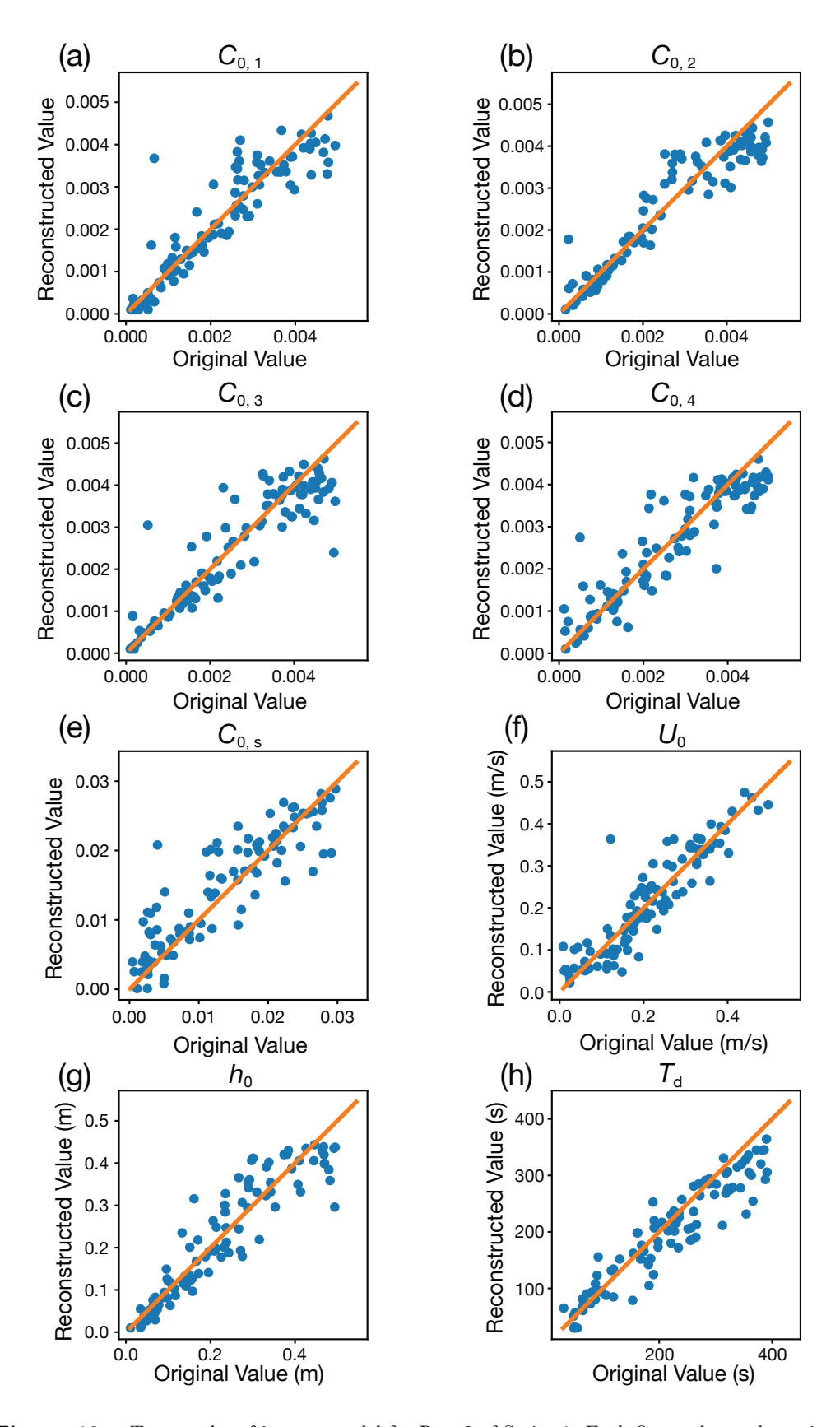


Figure 12. Test results of inverse model for Run 2 of Series 1. Each figure shows the estimation accuracy of the input parameters of the forward model. (a)–(d) Suspended sediment concentration of each grain-size class at the inlet. (e) Equivalent concentration at the inlet. (f) Flow velocity at the inlet. (g) Flow height at the inlet. (h) Flow duration.

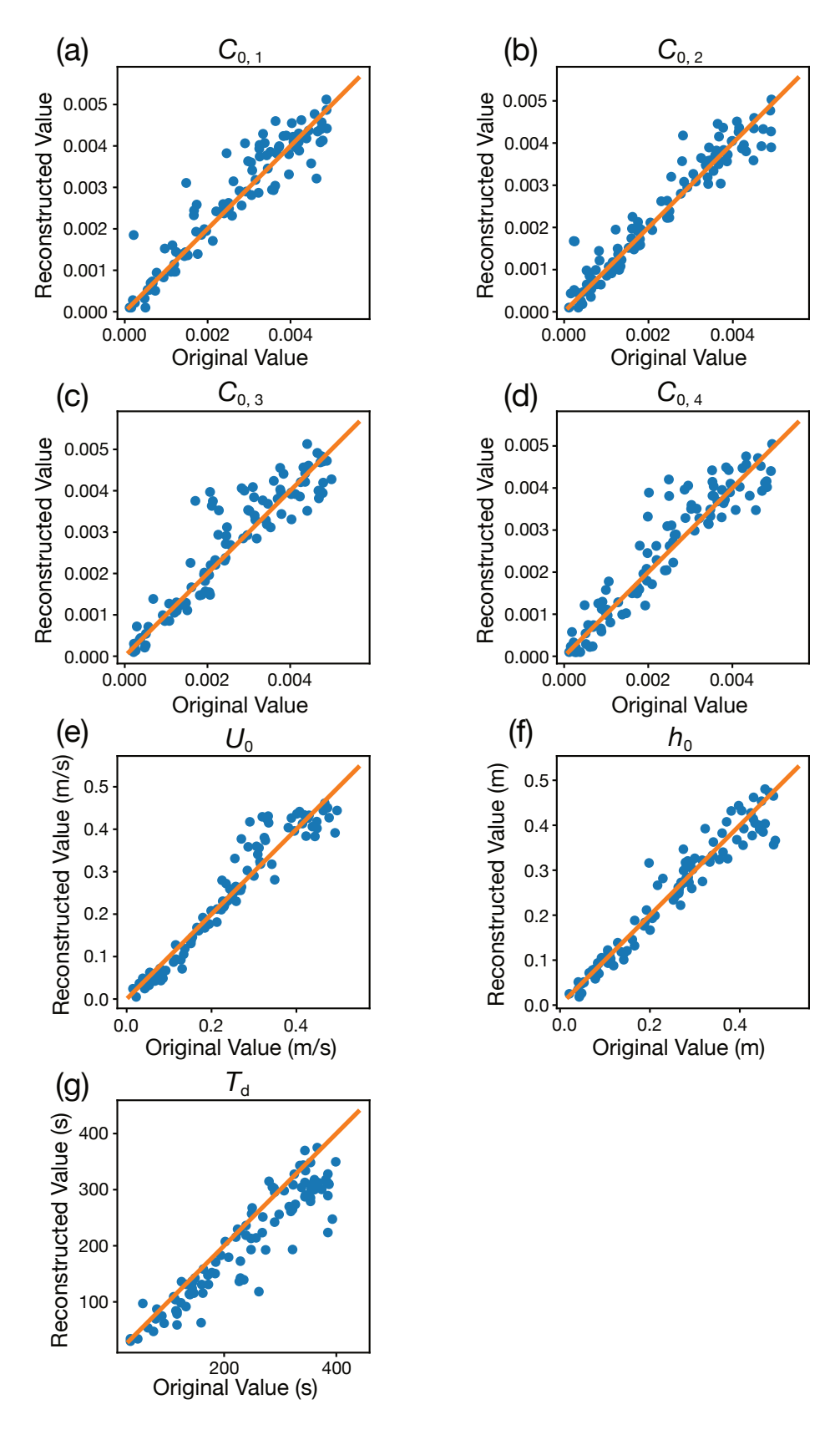


Figure 13. Test results of inverse model for Run 2 of Series 2. Each figure shows the estimation accuracy of the input parameters of the forward model. (a)–(d) Suspended sediment concentration of each grain-size class at the inlet. (e) Flow velocity at the inlet. (f) Flow height at the inlet. (g) Flow duration.

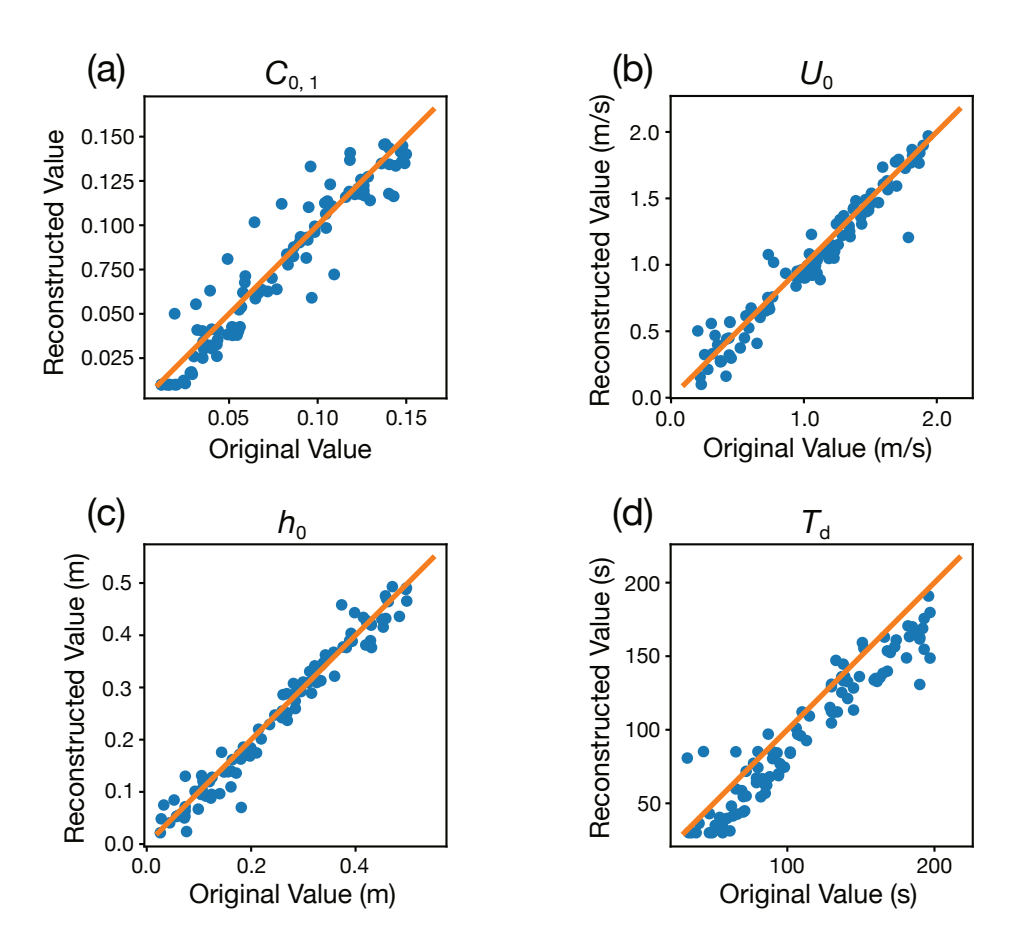


Figure 14. Test results of inverse model for Spychala et al. (2020). Each figure shows the estimation accuracy of the input parameters of the forward model. (a) Suspended sediment concentration of particles with $133\,\mu\mathrm{m}$ at the inlet. (b) Flow velocity at the inlet. (c) Flow height at the inlet. (d) Flow duration.

ized percentage errors of C_i ranged from 4.98% to 157%, which took a wider range of values than the other flow conditions (Tables 11, 12, 13).

Table 10. Model input parameters estimated by the inverse model applied to flume experiments.

	Series 1		Series 2	
	Run 1	Run 2	Run 2	Spychala et al. (2020)
$C_{0,1}$	0.00303	0.00365	0.00275	0.119
$C_{0,2}$	0.00285	0.00287	0.00192	-
$C_{0,3}$	0.00437	0.00310	0.00177	-
$C_{0,4}$	0.00310	0.00176	0.000579	-
$C_{0,\mathrm{s}}$	0.0201	0.000101	-	-
$U_0 (\mathrm{m/s})$	0.300	0.410	0.00501	0.781
$h_0\left(\mathrm{m}\right)$	0.0789	0.0654	0.420	0.0939
$T_{\rm d}\left({ m s}\right)$	188	285	404	54

Table 11. Comparison of measured and predicted flow conditions by inverse model in Series 1.

	Run 1			Run 2		
	Measured	Predicted	NPE (%)	Measured	Predicted	NPE (%)
C_1	9.66×10^{-4}	1.37×10^{-3}	34.9	5.71×10^{-4}	1.78×10^{-3}	102.7
C_2	6.81×10^{-4}	1.49×10^{-3}	74.4	4.65×10^{-4}	1.42×10^{-3}	101.4
C_3	5.54×10^{-4}	2.41×10^{-3}	125	4.78×10^{-4}	1.55×10^{-3}	105.5
C_4	2.08×10^{-4}	1.73×10^{-3}	157	3.87×10^{-4}	8.77×10^{-4}	77.6
$C_{ m T}$	2.41×10^{-3}	7.00×10^{-3}	97.6	1.90×10^{-3}	5.62×10^{-3}	98.5
U (m/s)	0.222	0.196	12.2	0.254	0.185	31.8
h (m)	0.2	0.0754	90.4	0.168	0.143	16.4
$T_{\rm d}$ (s)	116	188	47.3	113	285	86.3

In addition, the distributions of the experimental deposits were generally reconstructed well for Run 1 of Series 1, Run 2 of Series 2 of the present study, and Run 1 of Series 1 of the existing study; however, the reconstruction of Run 2 of Series 1 in this study was more challenging, as the condition was nearly bypassing flow (Figure 16, 17, 18, 19).

In Run 1 of Series 1, the channel-levee-like geomorphology was produced in both experimental and predicted topography (Figures 16a, 16b). As seen in the longitudinal section (along the A-A' line in Figure 16b), the topographic depression where almost no deposition occurred in the upstream area was well reproduced in the numerical prediction (Figure 16c). The predicted thick lobate deposits in the downstream region also matched the experimental result (Figure 16c). In addition, the cross-section (along the B-B' line in Figure 16b) showed similarity between the experimental and predicted topographies. The bed thickness was minimal in the central area, while two peaks were observed on both sides (Figure 16d).

The predicted topography for Run 2 of Series 2 also precisely reproduced the measured bed thickness (Figures 18a, 18b). The predicted bed thickness along the longitudinal profile (A-A' line in Figure 18b) agreed well with the measured bed thickness. It reproduced the characteristic of being thicker in the upstream region and thinner in the

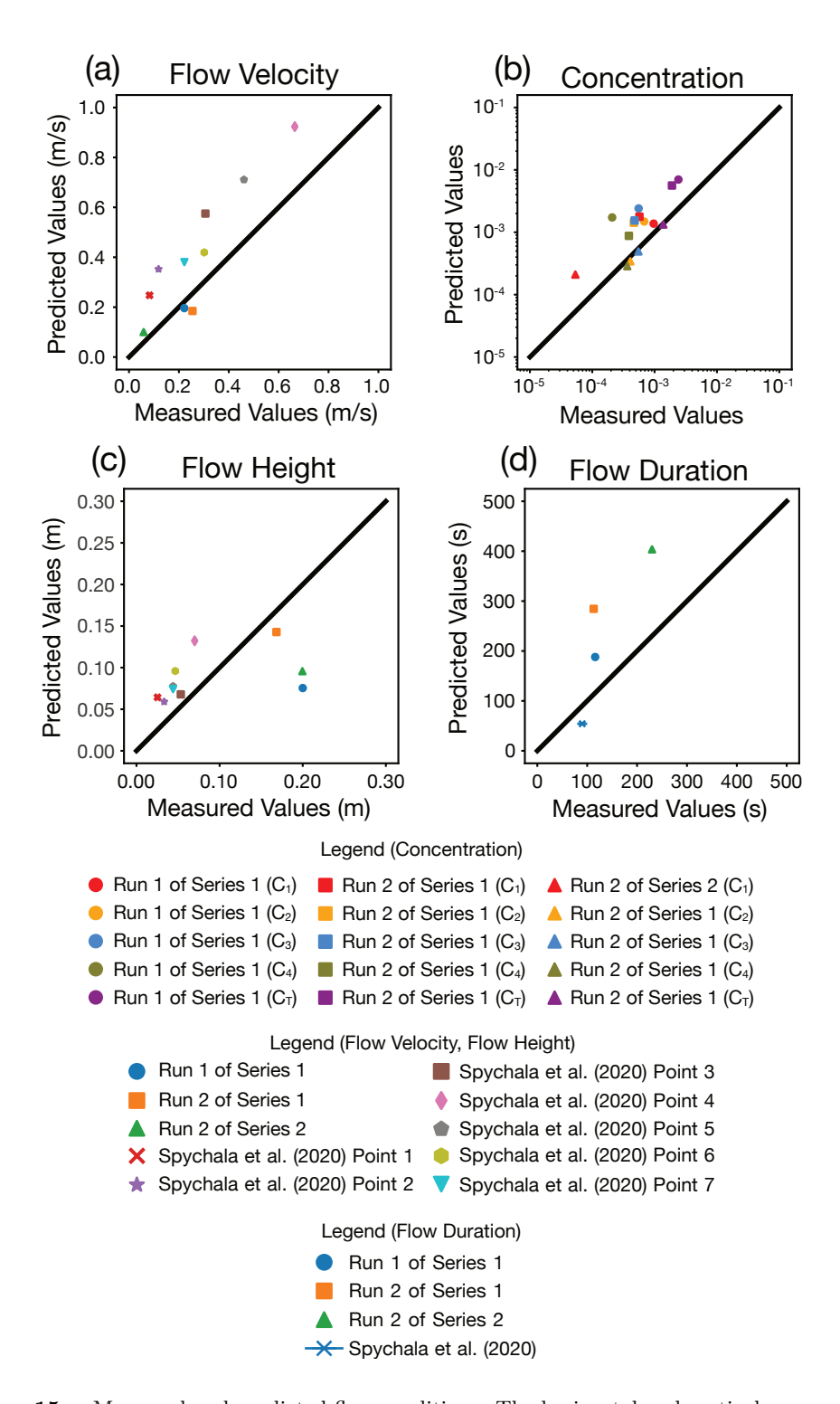


Figure 15. Measured and predicted flow conditions. The horizontal and vertical axes are the original and predicted values, respectively. A smaller deviation from the diagonal black line indicates a smaller error between the predicted and measured values. (a) Flow velocity. (b) Suspended sediment concentration. (c) Flow height. (d) Flow duration.

Table 12. Comparison of measured and predicted flow conditions by inverse model in Series 2.

	Measured	Predicted	NPE (%)
C_1	5.87×10^{-5}	3.96×10^{-4}	152
C_2	4.08×10^{-4}	5.97×10^{-4}	37.6
C_3	5.50×10^{-4}	8.65×10^{-4}	44.6
C_4	3.64×10^{-4}	3.35×10^{-4}	8.38
$C_{ m T}$	1.38×10^{-3}	2.19×10^{-3}	45.6
U (m/s)	0.0587	0.120	68.7
h (m)	0.200	0.0880	77.6
$T_{\rm d}$ (s)	230	404	54.8

Table 13. Comparison of measured and predicted flow conditions by inverse model in Spychala et al. (2020). The flow duration was reported as a range in Spychala et al. (2020), so the NPE is also calculated as a range. The subscript of number indicates the measurement point in the experiment (Figure 5).

	Measured	Predicted	NPE (%)	
$U_1 \text{ (m/s)}$	0.0823	0.248	100	
U_2 (m/s)	0.118	0.353	99.4	
$U_3 \text{ (m/s)}$	0.306	0.575	61.0	
$U_4 \text{ (m/s)}$	0.665	0.924	32.6	
$U_5 \text{ (m/s)}$	0.461	0.711	42.7	
$U_6 \text{ (m/s)}$	0.302	0.419	32.7	
$U_7 \text{ (m/s)}$	0.222	0.381	52.6	
h_1 (m)	0.0253	0.0643	86.9	
h_2 (m)	0.0333	0.0590	55.6	
h_3 (m)	0.0533	0.0679	24.0	
h_4 (m)	0.0700	0.132	61.6	
h_5 (m)	0.0440	0.0777	55.3	
h_6 (m)	0.04467	0.0959	69.1	
h_7 (m)	0.0440	0.0741	51.0	
$T_{\rm d}$ (s)	80-100	54	38.5 – 59.4	

Table 14. SMAPE values of predicted flow conditions from experimental deposits in the present study and in Cai and Naruse (2021).

	C_1	C_2	C_3	C_4	C_{T}	U	h	$T_{ m d}$
This study Cai and Naruse (2021)								

downstream region (Figure 18c). The predicted bed thickness along the cross-section (B-B' line in Figure 18b) also reproduced the feature of measured bed thickness, whose distribution exhibited a thicker deposit in the center, thinning laterally (Figure 18d).

The depositional feature observed in the experiment by Spychala et al. (2020) was also reconstructed well (Figure 19). The horizontal two-dimensional distribution of bed thickness was successfully predicted, including the eroded area inside the upstream channel and thick deposit at the channel terminus (Figures 19a, 19b). The bed thickness along the longitudinal section (A-A' line in Figure 19b) approximates the measured bed thickness (Figure 19c), and the cross section (B-B' line in Figure 19b) accurately captured the feature of the measured bed thickness, characterized by a thick deposit at the center and thinner deposits towards the edges (Figure 19d).

It was more challenging to reconstruct the distribution of the bed thickness in Run 2 of Series 1 than those in the other runs, while the channel-levee-like geomorphology was reproduced in the predicted topography (Figures 17a, b). The thicker deposits at the downstream area of the bypass zone occurred in both the measured and predicted results (Figures 17a–17d). Meanwhile, the predicted bed thickness was overestimated, more than ten times thicker than the measured values of bed thickness (Figure 17), which were 0–5 mm.

4 Discussion

4.1 Inverse Model Performance Verified with Artificial Datasets

The inverse models developed in this study were able to estimate the model input parameters with reasonable accuracy. The inversion results were particularly precise in the reconstruction of the second sediment concentration $C_{0,i}$, flow velocity U_0 , flow height h_0 , and flow durati

The inverse model performance protect that the characteristics of turbidites are sensitive to these flow conditions of turbidity currents. Indeed, the sensitivity tests of the forward model, as well as previous studies, suggested that these parameters have a substantial influence on the depositional features (Figures 8, 9), consistent with the inversion verification results. In the sensitivity test, increasing the suspended sediment concentration at the inlet and extending the flow duration resulted in a thick deposition near the inlet. The same trend was observed in experimental runs in past studies (e.g., Garcia, 1994). The experiments in Poppeschi et al. (2023) exhibited that a high flow velocity at the inlet caused a large bypass zone near the inlet, as observed in the sensitivity test in this study. In Ge et al. (2018), three-dimensional simulations of turbidity currents were performed on a field scale. Their results indicated that the deposit thickness increases as the flow height increases. Judging from the geomorphological responses to the flow conditions of the experimental and field-scale currents, the inverse modeling approach proposed in this study can be expected to estimate those hydraulic conditions from the actual turbidites within a reasonable range of errors.

The only parameter that was challenging to estimate was the equivalent sediment concentration for saline water $C_{0,s}$, which served as an analog to washloads in the actual flows. Reconstruction of this parameter exhibited larger errors than the other parameters (Figures 11e, 12e; Table 7), consistent with the sensitivity test exhibiting that the saline density is less influential on the depositional characteristics, as shown in Figures 8c–8e and 9. Although the washloads, which are fine-grained and do not remain as sediment, affect the flow dynamics in terms of fluid density, they have a negligible effect on the topography. The actual turbidity currents that transport fine-grained materials and have high flow velocities often bypass the upstream regions without leposition (Peakall et al., 2000; Rowland et al., 2010; Stevenson et al., 2013). Thus, inverse nodels inevitably fail to accurately estimate conditions for bypassing flows.

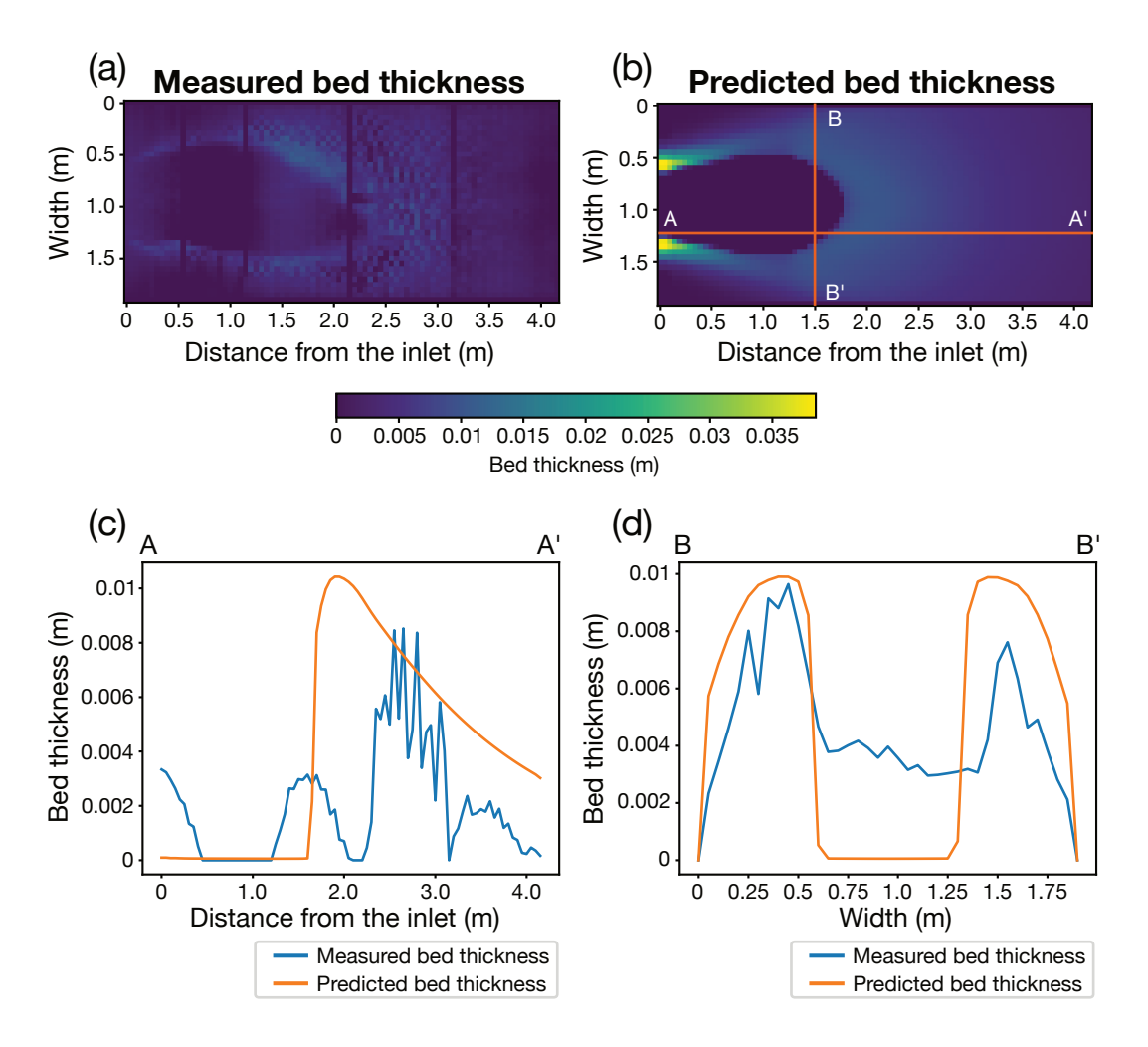


Figure 16. Measured and predicted bed thickness of Run 1 of Series 1. (a) 2D horizontal distribution of the measured deposit. (b) 2D horizontal distribution of the predicted deposit. (c) A-A' cross-section of the predicted and measured bed thicknesses. (d) B-B' cross-section of the predicted and measured bed thicknesses.

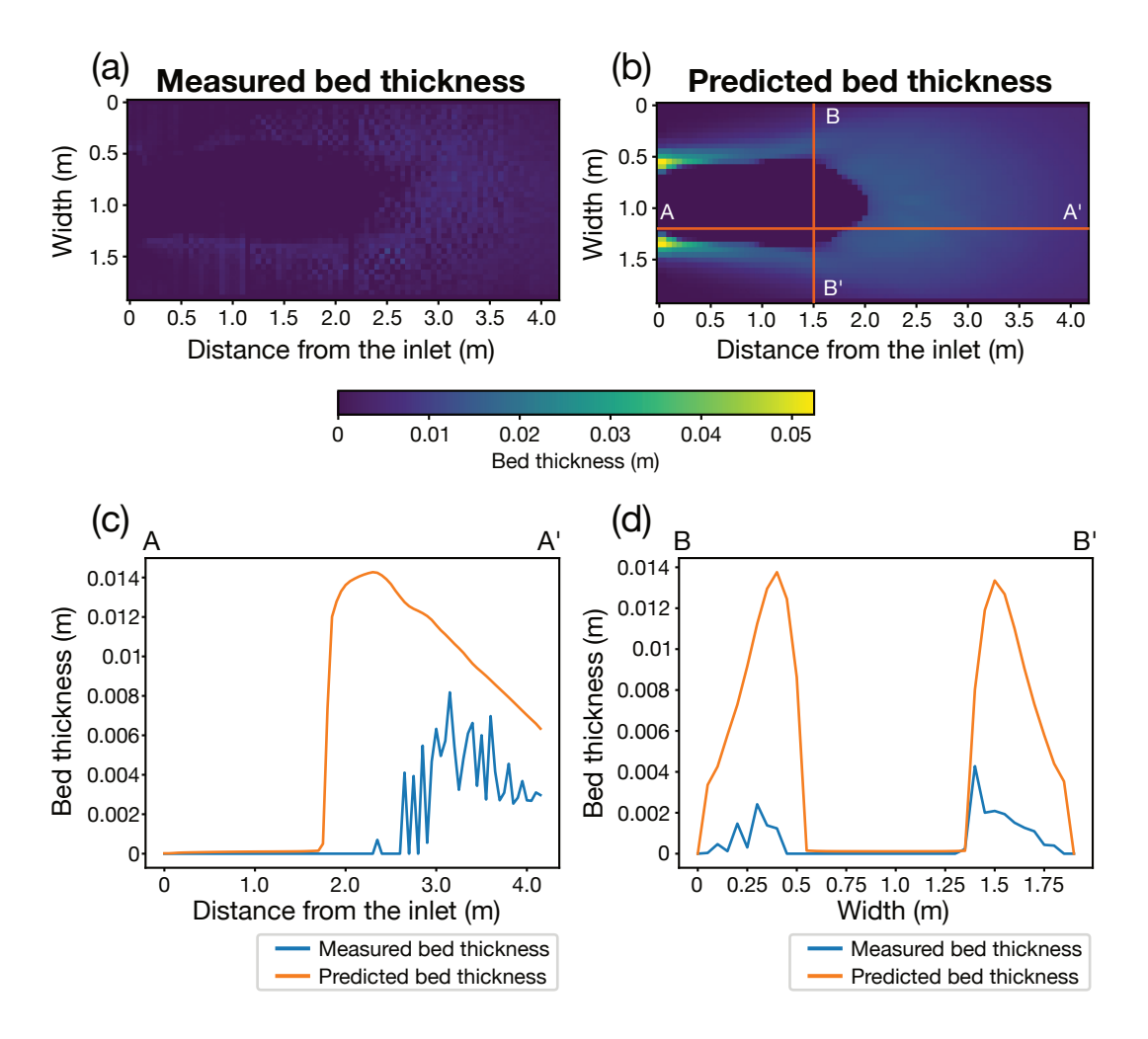


Figure 17. Measured and predicted bed thickness of Run 2 of Series 1. (a) 2D horizontal distribution of the measured deposit. (b) 2D horizontal distribution of the predicted deposit. (c) A-A' cross-section of the predicted and measured bed thicknesses. (d) B-B' cross-section of the predicted and measured bed thicknesses.

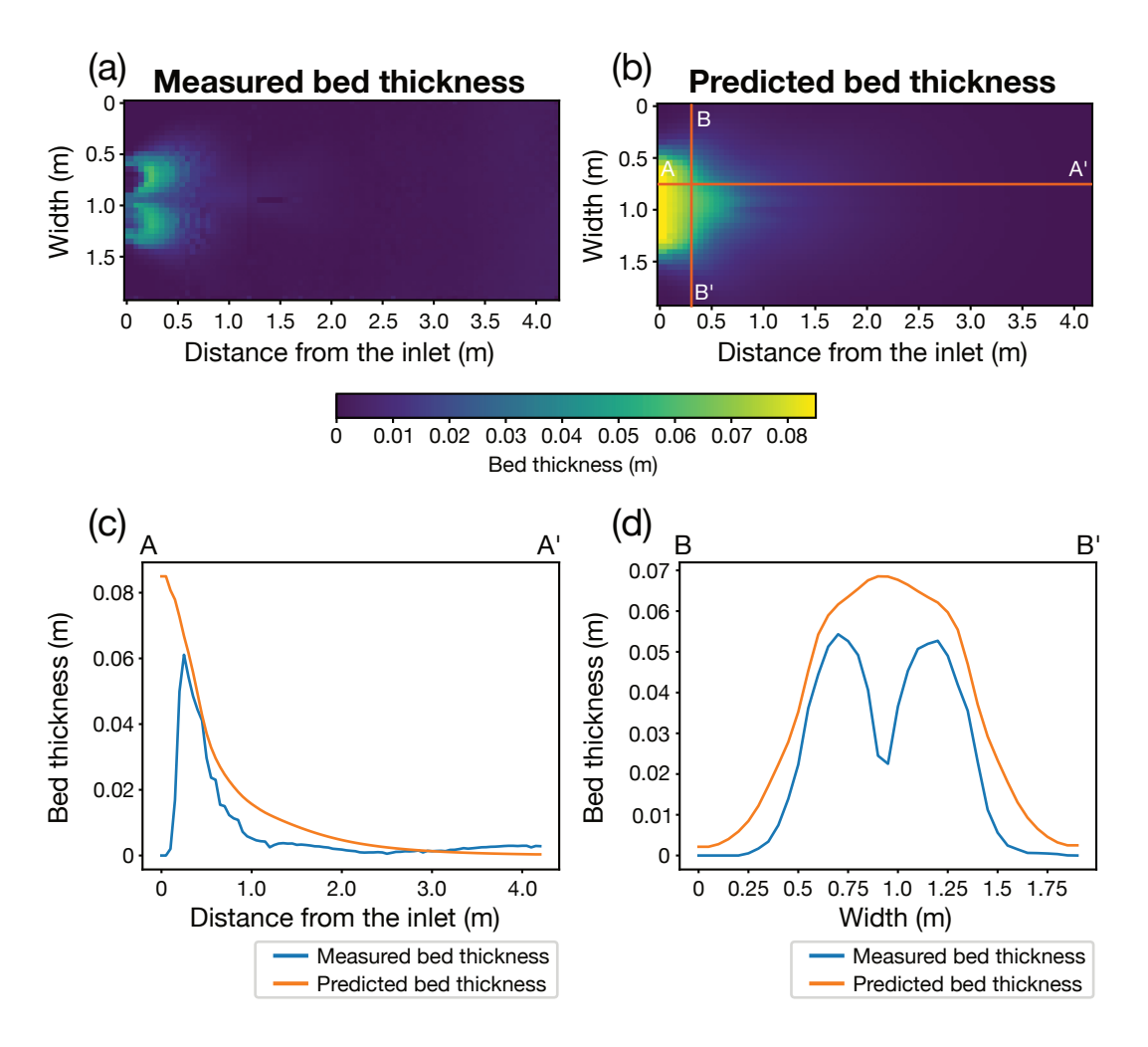


Figure 18. Measured and predicted bed thickness of Run 2 of Series 2. (a) 2D horizontal distribution of the measured deposit. (b) 2D horizontal distribution of the predicted deposit. (c) A-A' cross-section of the predicted and measured bed thicknesses. (d) B-B' cross-section of the predicted and measured bed thicknesses.

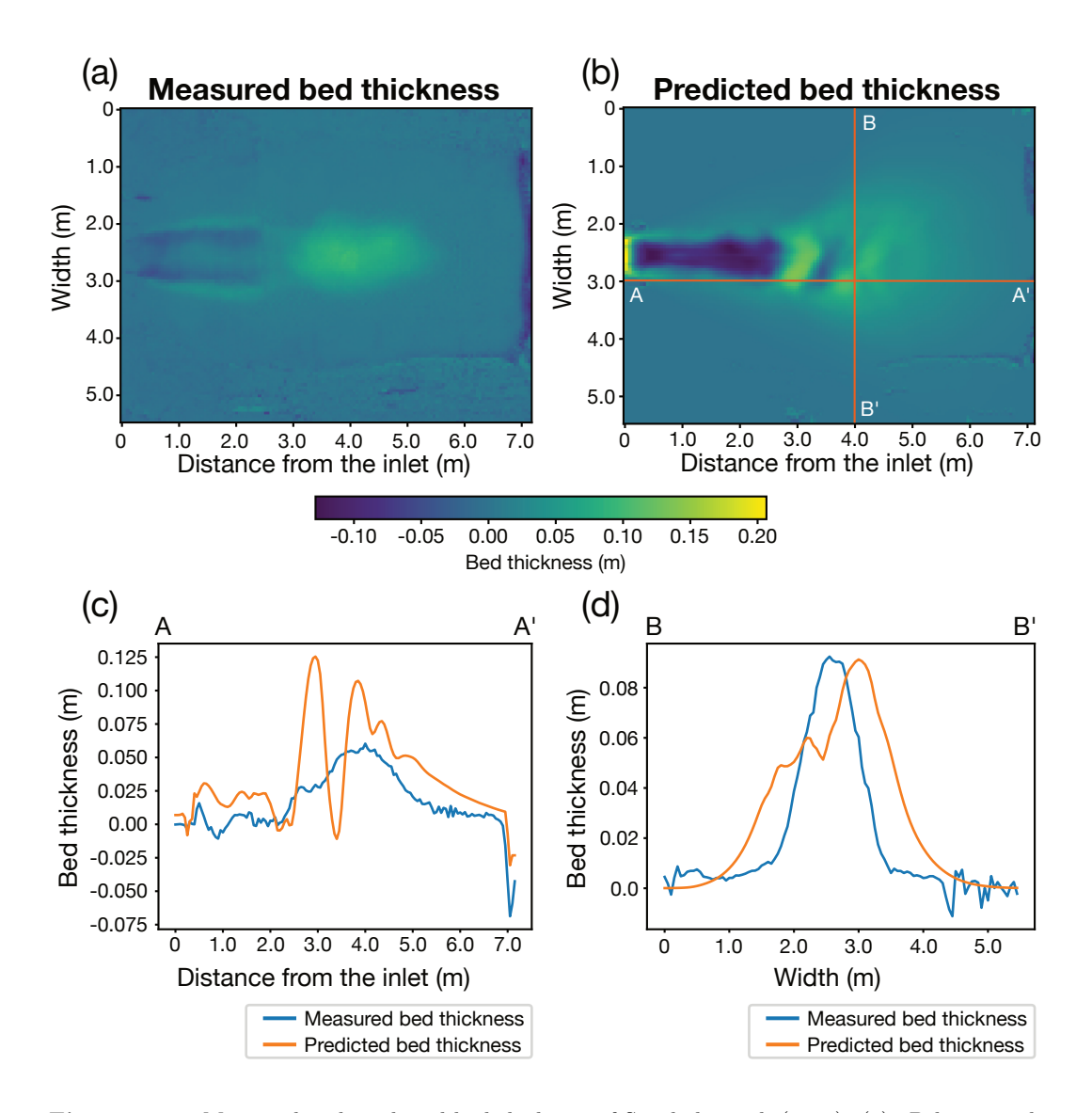


Figure 19. Measured and predicted bed thickness of Spychala et al. (2020). (a) 2D horizontal distribution of the measured deposit. (b) 2D horizontal distribution of the predicted deposit. (c) A-A' cross-section of the predicted and measured bed thicknesses. (d) B-B' cross-section of the predicted and measured bed thicknesses.

4.2 Inversion of Experimental Turbidity Currents

705

706

707

708

709

710

711

712

714

715

716

718

719

720

721

722

723

726

727

728

730

731

732

734

735

738

739

740

741

742

743

746

747

748

750

751

752

753

The proposed two-dimensional inverse model of turbidity currents demonstrated reasonable performance even over complex topography, in contrast to the previous one-dimensional models (e.g., Cai & Naruse, 2021), which were limited to flat topography. The SMAPE values of C_i and C_T (64.5%–86.2%) were lower than those of the previous 1D inverse model developed by Cai and Naruse (2021) (76.2% –113%). The SMAPE values of the flow velocity U, flow height h, and flow duration T_d in this study (51.7 to 62.0%) were also nearly equivalent to those in the previous study (24.2–43.1%). These results highlight the practical applicability and improved robustness of the proposed 2D inverse model in reconstructing turbidity current dynamics over complex seabed topography.

The possible origins of the estimation errors were the measurement accuracy of the experimental conditions. The extrapolation of vertical profiles of the parameters to obtain the layer-averaged flow conditions can also potentially cause measurement errors. This study also estimated the layer-averaged flow velocities and flow heights in Run 1 of Series 1 and the experiment of Spychala et al. (2020) using the empirical formula proposed by Altinakar et al. (1996) (Equation 6 and 8). However, (Sequeiros et al., 2010) pointed out that the ratio $U_{\rm max}/U$ and $h_{\rm m}/h$ in supercritical flows ranges from 1.36 to 1.60 and 0.165 to 0.628, respectively, which can cause the measurement uncertainty ranging from -4.41% to -18.7% in flow velocities and from -52.2% to 81.8% in flow heights. The predictions in the layer-averaged concentrations tend to exhibit larger errors at the grain size classes with very low concentrations (e.g., C_3 and C_4 in Run 1 of Series 1, and C_1 in Run 2 of Series 2). These errors could be attributed to the difficulty in measuring small sample amounts in siphon-sampled specimens.

The uncertainties of the forward model can also contribute to the difference between the predicted and measured values. The four-equation model employed in this study assumed that the values of flow velocity, suspended sediment concentration, and turbulent kinetic energy are constant in the region $0 \le z \le h$ (i.e., "top-hat" assumption) (Parker et al., 1987). However, Parker et al. (1986) indicated that the shape factors obtained from the experimental flow differed from the values (unity or zero) assumed in the model by -38% to 18%. The other experimental studies (Parker et al., 1987; Islam & Imran, 2010; Sequeiros et al., 2010) also obtained values that deviated from the top-hat assumption, ranging from -54% to 45%. Skevington and Dorrell (2025) reported that the shape factors obtained from experimental and natural turbidity currents datasets were concentrated in significantly different values from the top-hat assumption. The shape factor, with an extensive range of measurements, is r_0 , which is defined as the ratio of the nearbed sediment concentration to the layer-averaged concentration. This value affects the settling rates of sediment. This study set this parameter to be 2.0 based on Kostic and Parker (2006), while Skevington and Dorrell (2025) showed that r_0 can take a range from about 0.8 to 5.0. As pointed out by Dorrell et al. (2014), these shape factors affect the model predictions of all flow parameters. A numerical model of turbidity currents that considers arbitrary shape factors Skevington and Dorrell (2025) is expected to overcome these issues, thereby improving the performance of the inverse model in future studies.

Despite various potential sources of uncertainty in measurements and modeling described above, the inverse model developed in this study effectively estimated flow conditions within an acceptable margin of error (SMAPE < 100%), demonstrating its suitability for reconstructing approximate turbidity current dynamics from depositional records.

4.3 Reproducibility of depositional features from inversion results

The inverse models developed in this study successfully reconstructed the experimental depositional features from the estimated model input parameters, proving that the model adequately captured the flow morphodynamic behaviors. The predicted bed thickness distributions approximated most of the experimental results except for Run

1 of Series 2 (Figures 16, 17, 18, 19). Fine topographic features, such as ripples, were not reproduced because the shallow water equations employed in the forward model of this study average velocity and suspended sediment concentration in the depth direction, assuming the long-wave approximation for flow dynamics. In addition, two mounds were formed in the upstream region of Run 2 of Series 2, but the model did not reproduce them. These mounds were caused by the heterogeneous distribution of the flow velocity in the width direction at the inlet (Poppeschi et al., 2023), which was not considered in the model calculations.

The discrepancy between the predicted and measured bed thickness in Run 2 of Series 1 was probably caused by the bypassing conditions of the flow. The bed thickness of this experiment was only about 1 mm on average; thus, the sediment was almost bypassed. Under such conditions, accurately reproducing the flow conditions and the geometry of the deposits would not be easy even with an adequately trained inverse model. This result is consistent with the testing results of the artificial datasets discussed in Section 4.1, indicating that inverse analysis is difficult if the suspended sediment is not sufficiently preserved in the deposit, as pointed out in a previous study (Naruse & Nakao, 2021).

The inversion framework proposed in this study can potentially be utilized for estimating the spatial distribution of ancient deposits. Indeed, the inverse model predicted the two-dimensional distribution of bed thickness only from the limited sampling points. In general, it is challenging to estimate spatial distributions of ancient turbidites because of the limited number of available outcrops and coring sites. However, suppose the paleohydraulic conditions of turbidity currents are estimated by inverse analysis, the forward model can reconstruct the flow behavior of turbidity currents outside the surveyed area, thereby obtaining the entire geometry of turbidites. Such estimates of the distributions of coarse-grained deposits are essential for addressing the economic demands of carbon capture and storage and hydrocarbon exploration (Nygård et al., 2006; Maiorana et al., 2024).

4.4 Applicability to Field Data

Although the two-dimensional inverse model proposed in this study was applied to turbidity currents flowing over complex topography, no significant performance degradation was observed compared to the one-dimensional inverse model in the previous study (Cai & Naruse, 2021), which considers turbidity currents flowing on a flat bed in a straight channel. Therefore, the inverse model developed in this study can be applied to the currents flowing over the natural complex topography at the deep-sea floor, such as the trench slope at an active margin and the minibasins formed by salt diapirs at a passive margin.

The DNN-based 2D inverse model developed in this study is more efficient and yields reasonable results for field data than other optimization methods. Most previous studies have employed optimization methods that require iterative computation for inverse analyses of gravity currents, such as the genetic algorithm (Nakao et al., 2020), the Markov Chain Monte Carlo method (Moretti et al., 2020; Kameda & Okamoto, 2021), the surrogate management method (Lesshafft et al., 2011), and the adjoint method (Parkinson et al., 2017). However, these optimization methods have high computational loads because they require many iterations. In addition, the results of the optimization methods are not always reasonable. For example, Parkinson et al. (2017) estimated the flow thickness of a turbidity current from the actual turbidite bed as 0.00192 m or 3950 m because the oversimplified assumptions for the forward model needed to iterate the model calculations. In contrast, the inverse model developed in this study can perform inverse analysis almost instantly once the training process is complete, yielding reasonable results. Although the production of the training datasets takes a relatively long time, the

forward model computation in this procedure can be entirely parallelized, allowing the models with high computational load to be employed in our inversion framework. Therefore, the 2D inverse model developed in this study is more suitable for the field-scale turbidity current than previous inverse methods, which employed classical optimization methods.

The primary feature of the inverse analysis framework in this study is that it allows easy modification of the forward model to a formulation that is more suitable for the field conditions. Since the inverse model is trained on datasets generated by the forward model, improving the forward model can improve the performance of the inverse model. For example, a two-layer model that reproduces long-runout turbidity currents was recently proposed (Ma et al., 2025). Turbidity currents traveling over 1130 km have been observed in the Congo Submarine Canyon and its associated channel (Talling et al., 2022); however, a single-layer model is difficult to predict such behavior of turbidity currents flowing over a long distance, as they decelerate due to the entrainment of the surrounding water. A two-layered formulation, where the lower driving and upper dilute layers comprise a turbidity current, can predict the long-runout flows because the ambient water entrainment occurs only in the dilute layer, and the main driving force of the flow is maintained in the lower layer. Therefore, it is appropriate to use a two-layer model for performing inversion for large-scale submarine geomorphology. Not limited to such cases, the inverse model framework proposed in this study is open to employing various types of forward models.

5 Conclusions

This study developed horizontal two-dimensional inverse models based on a deep neural network (DNN) to estimate turbidity currents flow parameters from turbidite characteristics. Validation with synthetic datasets demonstrated that the inverse models successfully estimated most input parameters with a symmetric mean absolute percentage error (SMAPE) below 32.5% and minimal biases, except for the layer-averaged density-equivalent sediment concentration for saline water $C_{0,s}$. The difficulty in estimating $C_{0,s}$ in Series 1 likely stems from its limited imprint on the resulting deposit.

The inverse model also reconstructed the flow conditions of the experimental turbidity currents with reasonable accuracy. The normalized percentage error (NPE) of the layer-averaged suspended sediment concentration and total suspended sediment concentration ranged from 4.98% to 157%, and from 45.6% to 98.5%, respectively. For flow velocity and height, the NPEs ranged from 12.2% to 100% and 24.0% to 90.4%, while the NPE of flow duration ranged from 38.5% to 86.3%. The SMAPE values for suspended sediment concentration were comparable to those reported by Cai and Naruse (2021). Although the SMAPE values for flow velocities, heights, and durations were slightly higher than those of the previous one-dimensional inverse model, they remained within acceptable ranges, considering uncertainties such as profile extrapolation, sampling disturbance, and forward model assumptions.

The spatial distribution of the bed thickness was also well reproduced. In Run 1 of Series 1, the forward model calculation using the estimated conditions successfully reconstructed a channel-levee-like deposit. In Run 2 of Series 2, it captured the general trend of thick upstream deposits and thinner downstream deposits. Furthermore, the model accurately reconstructed the deposits of the experiment by Spychala et al. (2020), including the upstream channel erosion and the thick terminal deposits. Although the bed thickness was slightly overestimated in Run 2 of Series 2 due to the thinness of the deposits, the characteristic morphology was still reasonably reproduced.

Overall, the proposed horizontally two-dimensional inverse model achieved performance comparable to that of the previous one-dimensional DNN-based model while of-

fering substantially lower computational cost than the conventional optimization-based methods. This demonstrates the efficiency and practical applicability of the model to field-scale inverse analysis. Since the proposed inverse model framework is independent of the choice of forward models, it can be readily adapted to incorporate more advanced numerical models. This flexibility suggests that the method can be extended to reliably reconstruct field-scale flows over complex topography.

Appendix A Generation of the digital elevation models

To obtain the digital elevation models (DEMs) by the structure from motion (SfM) technique (Fonstad et al., 2013), the experimental topographies in the flume were photographed before and after each run. The images were captured using a waterproof digital camera (OM SYSTEM TOUGH TG-6 and TOUGH TG-7) in subaqueous positions without draining water to avoid topographic deformation. To take clear underwater images, the flume was left untouched for 2–3 days after the experimental run before taking photographs. Colored sands were spread over the experimental deposits to add the reference points of images to be used in the SfM method. The spatial interval between the acquisition of images was 0.15 m in the longitudinal direction and 0.1 m in the lateral direction of the flume. The camera angle was changed to three different positions to capture the three-dimensional geometry of the topography. As a result, in Series 1, 978 and 844 photographs were taken for Runs 1 and 2, respectively. In Series 2, 2868 and 1937 photographs were taken for Runs 1 and 2, respectively.

Subsequently, three-dimensional point clouds representing the elevation of the experimental topography were produced using the subaqueous photographs. The commercial software Agisoft Metashape 1.8.4 was used to generate point clouds. To guarantee the accuracy of the topographic elevations, the ground control points (GCPs) were set on the side of the flume (Figure A1; Table A1), and the coordinates of those GCPs were given to the software for the SfM analysis. All GCPs were used to reconstruct the topography in Series 1. In Series 2, however, the GCP 1–1 located on the right-bank side of the upstream end was not used in the analysis because this GCP marker toppled over during the experiment.

Preprocessing, including outlier removal, was conducted to ensure the reliability of the point-cloud data. Since the point cloud near the inlet was sparse due to the difficulty in the image references by the light reflection, only the point cloud data after 0.35 m from the upstream end was used in Series 1. The outlier points were removed after generating point clouds using the k-nearest neighbor algorithm (Cover & Hart, 1967). Python 3.7 and Open3D 0.11.2 packages were used for this purpose. The number of the neighbor points K to judge the outlier points was set to 100 in Series 1 and 500 in Series 2, and the threshold coefficient m for the standard deviation of the elevation was set to 0.1 in this study.

Finally, DEMs were created from the point-cloud datasets. Before producing the DEM, the voxel downsampling procedure was applied to the point cloud dataset to reduce the excessive information. The point clouds composed of a large number of points were summarized into a limited number of collections of points averaged for every sampling boxes (i.e., voxel) by this procedure. The voxel size was 0.001 m in both series. Following this, the radial basis function (RBF) interpolation was performed with SciPy 1.7.3 to produce the digital elevation model with a constant grid spacing of 0.001 m in both series.

Table A1. Coordinates of Ground Control Points.

	1-1	1-2	2-1	2-2	3-1	3-2	4-1	4-2	5-1	5–2
\overline{x}	0	0	0.9	0.9	1.5	1.5	2.5	2.5	3.5	3.5
y	0	1.9	0	1.9	0	1.9	0	1.9	0	1.9
z	0.565	0.575	0.480	0.465	0.415	0.415	0.375	0.370	0.32	0.325

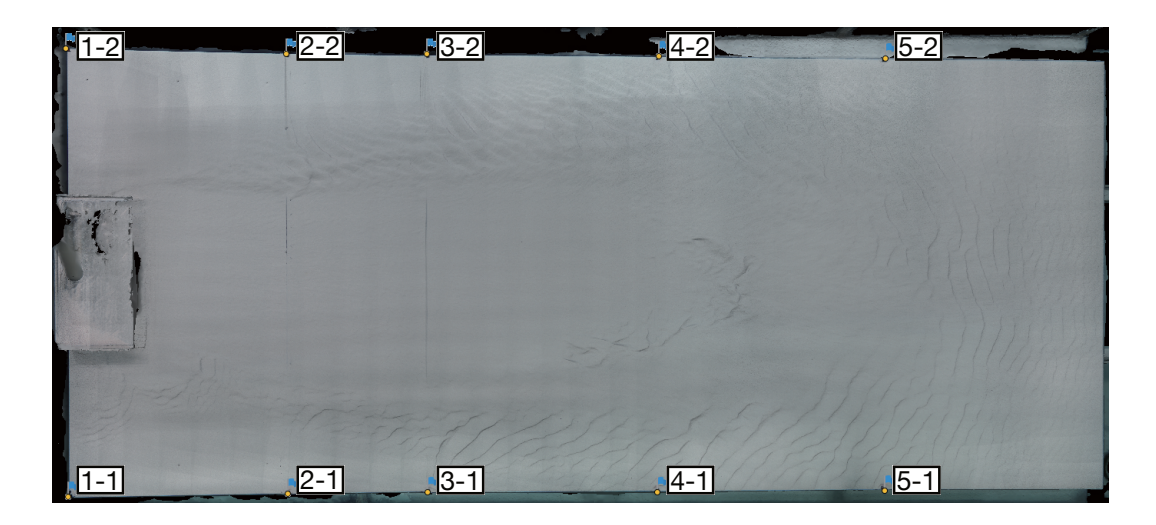


Figure A1. Location of ground control points.

Notation

903

904

905

- c_i Time-averaged flow velocity
- $M_{\mathbf{w}}$ Mass of fluid
- $M_{
 m s}$ Mass of suspended sediment
- $F_{\mathrm{s}i}$ Fraction of the *i*th grain-size class in sampled suspended sediment
- $ho_{\mathbf{f}}$ Density of fluid
- $\rho_{\rm s}$ Density of sediment particle
- U Layer-averaged flow velocity in x-direction
 - V Layer-averaged flow velocity in y-direction
 - C_i Layer-averaged suspended sediment concentration of ith grain-size class
- C_{T} Layer-averaged total suspended sediment concentration
- h Flow height
- z Height above the bed
 - $U_{\rm max}$ Maximum value of vertical flow velocity profile
- $c_{\mathbf{b}i}$ Suspended sediment concentration of ith grain-size at 0.05h,
- $h_{
 m m}$ Height above the bed at which the flow velocity reaches $U_{
 m max}$
- $C_{
 m s}$ Layer-averaged density-equivalent sediment concentration for saline water
- $c_{
 m s}$ Density-equivalent sediment concentration for saline water
- $\rho_{\mathbf{w}}$ Density of fresh water
- $ho_{\mathbf{sw}}$ Density of saline water
- R Submerged specific density of sediment particles
- $Fr_{\mathbf{d}}$ Densimetric Froude number
- $ho_{
 m t}$ Density of turbidity current
- g Gravity acceleration
- Re Reynolds number

```
\tau_i^* Shields number
929
        	au_{\mathbf{c}i}^* Critical Shields number of ith grain-size class
930
        D_{si} Grain diameter of sediment particles of ith grain-size class
        c_{\mathbf{f}} Friction coefficient
932
        \kappa Karman constant
933
        k_{\rm s} Roughness height
934
        D_{\rm s50} Mean grain diameter
935
        Re_{pi} Particle Reynolds number
        \eta_i Sediment volume per unit area for ith grain-size class
937
        V_{si} Sediment volume fraction of ith grain-size class at sampling point
938
       \eta_{\rm T} Bed thickness
       t Time
940
        \boldsymbol{x} Bed-attached horizontal coordinate
941
       y Bed-attached horizontal coordinate
        K Layer-averaged turbulent kinetic energy
943
        F_i Volume fraction of the ith grain-size class in active layer
        e_{\mathbf{w}} Entrainment rates of ambient water
945
            Entrainment rates of basal sediment of ith grain-size class
946
        w_{si} Settling velocity of a sediment particle of ith grain-size class
947
       \nu_{\rm t} Horizontal eddy viscosity
948
        \epsilon_0 Dissipation rate of turbulent kinetic energy
       \lambda_{\mathbf{p}} Porosity of bed sediment
950
        r_0 Ratio of the near-bed concentration to layer-averaged concentration
951
        L_{\mathbf{a}} Thickness of active layer
       u_* Friction velocity
953
        R_i Bulk Richardson number
        U_0 Layer-averaged flow velocity at inlet
        C_{0,i} Layer-averaged concentration of ith grain-size class at inlet
956
        C_{0,s} Layer-averaged density-equivalent sediment concentration for saline water at in-
957
958
        h_0 Flow height at inlet
959
       T_{\rm d} Flow duration
960
```

Data Availability Statement

962

963

964

965

966

967

971

972

973

 ν Kinematic viscosity of water

The training and test datasets for the inversion model, the inversion results, the flume experiment results, and the scripts used to produce the figures from the data are available from Zenodo at https://doi.org/10.5281/zenodo.16751886 under the Creative Commons Attribution 4.0 International license (Fujishima, 2025). The nninv1d used to develop the DNN-based inverse models in this study is a modified version of the one used in (Naruse & Nakao, 2021), adapted specifically for the purposes of this research. The version of 1.0.0 of nninv1d (Fujishima & Naruse, 2025a) used in this study is archived at https://doi.org/10.5281/zenodo.16731283. The source code of nninv1d is available under MIT Licence and is openly maintained at https://github.com/fujishimaseiya/nninv1d. The version 1.0.0 of turb2d (Fujishima & Naruse, 2025b) used for forward model calcuation is preserved at https://doi.org/10.5281/zenodo.16730833, available via MIT Licence and developed openly at https://github.com/fujishimaseiya/turb2d.

Acknowledgments

We would like to thank Prof. Ubukata, Prof. Sato, and the members of the Biosphere group at Kyoto University for their valuable suggestions and discussions. We also gratefully acknowledge Prof. Spychala (RWTH Aachen University) for providing the flume experiment datasets. This work was supported by JST, the establishment of university fellowships towards the creation of science technology innovation (Grant Number JP-MJFS2123), and JST SPRING (Grant Number JPMJSP2110). Additional supports were provided by the Sediment Dynamics Research Consortium, sponsored by JAPEX, JOG-MEC, and INPEX. This work was also supported by the Iwadare Scholarship Foundation.

References

- Altinakar, M., Graf, W., & Hopfinger, E. (1996). Flow structure in turbidity currents. *Journal of Hydraulic Research*, 34(5), 713–718. doi: https://doi.org/10.1080/00221689609498467
- Arai, K., Naruse, H., Miura, R., Kawamura, K., Hino, R., Ito, Y., ... others (2013). Tsunami-generated turbidity current of the 2011 tohoku-oki earthquake. *Geology*, 41(11), 1195–1198. doi: https://doi.org/10.1130/G34777.1
- Bent, A. L. (1995). A complex double-couple source mechanism for the ms 7.2 1929 grand banks earthquake. Bulletin of the Seismological Society of America, 85(4), 1003-1020. doi: https://doi.org/10.1785/BSSA0850041003
- Cai, Z. (2022). Reconstructing the behavior of turbidity currents from turbiditesreference to anno formation and japan trench (PhD thesis, Kyoto University). doi: https://doi.org/10.14989/doctor.k24174
- Cai, Z., & Naruse, H. (2021). Inverse analysis of experimental scale turbidity currents using deep learning neural networks. Journal of Geophysical Research: Earth Surface, 126(8), e2021JF006276. doi: https://doi.org/10.1029/2021JF006276
- Clevert, D.-A., Unterthiner, T., & Hochreiter, S. (2016). Fast and accurate deep network learning by exponential linear units (elus). doi: https://doi.org/10.48550/arXiv.1511.07289
- Cover, T., & Hart, P. (1967). Nearest neighbor pattern classification. IEEE Transactions on Information Theory, 13(1), 21-27. doi: https://doi.org/10.1109/TIT.1967.1053964
- Dorrell, R. M., Darby, S. E., Peakall, J., Sumner, E. J., Parsons, D. R., & Wynn, R. B. (2014). The critical role of stratification in submarine channels: Implications for channelization and long runout of flows. Journal of Geophysical Research: Oceans, 119(4), 2620-2641. doi: https://doi.org/10.1002/2014JC009807
- Duchi, J., Hazan, E., & Singer, Y. (2011). Adaptive subgradient methods for online learning and stochastic optimization. *Journal of Machine Learning Research*, 12(61), 2121–2159.
- Ellison, T., & Turner, J. (1959). Turbulent entrainment in stratified flows. *Journal of Fluid Mechanics*, 6(3), 423–448. doi: https://doi.org/10.1017/S0022112059000738
- Falcini, F., Marini, M., Milli, S., & Moscatelli, M. (2009). An inverse problem to infer paleoflow conditions from turbidites. *Journal of Geophysical Research:* Oceans, 114(C10). doi: https://doi.org/10.1029/2009JC005294
- Ferguson, R., & Church, M. (2004). A simple universal equation for grain settling velocity. *Journal of Sedimentary Research*, 74(6), 933–937. doi: https://doi.org/10.1306/051204740933
- Fonstad, M. A., Dietrich, J. T., Courville, B. C., Jensen, J. L., & Carbonneau, P. E. (2013). Topographic structure from motion: a new development in photogrammetric measurement. *Earth Surface Processes and Landforms*, 38(4), 421-430.

doi: https://doi.org/10.1002/esp.3366

- Fujishima, S. (2025, 8). Dataset for the experimental verification of a dnn-based horizontal two-dimensional inverse model [dataset]. Zenodo. doi: https://doi.org/10.5281/zenodo.16751886
- Fujishima, S., & Naruse, H. (2025a, 8). nninv1d (version 1.0.0) [software]. Zenodo. doi: https://doi.org/10.5281/zenodo.16731283
- Fujishima, S., & Naruse, H. (2025b, 8). turb2d (version 1.0.0) [software]. Zenodo. doi: https://doi.org/10.5281/zenodo.16730833
- Garcia, M. H. (1994). Depositional turbidity currents laden with poorly sorted sediment. *Journal of Hydraulic Engineering*, 120(11), 1240-1263. doi: https://doi.org/10.1061/(ASCE)0733-9429(1994)120:11(1240)
- Garcia, M. H. (2008). Sediment transport and morphodynamics. In Sedimentation engineering (p. 21-163). doi: https://doi.org/10.1061/9780784408148.ch02
- Ge, Z., Nemec, W., Gawthorpe, R. L., Rotevatn, A., & Hansen, E. W. M. (2018). Response of unconfined turbidity current to relay-ramp topography: insights from process-based numerical modelling. Basin Research, 30(2), 321-343. doi: https://doi.org/10.1111/bre.12255
- Hirano, M. (1971). On riverbed variation with armoring. In *Proceedings of the japan society of civil engineers* (Vol. 195, pp. 55–65). doi: https://doi.org/10.2208/jscej1969.1971.195_55
- Hiscott, R. N. (1994). Loss of capacity, not competence, as the fundamental process governing deposition from turbidity currents. *Journal of Sedimentary Research*, 64(2a), 209-214. doi: https://doi.org/10.2110/jsr.64.209
- Hsu, S.-K., Kuo, J., Chung-Liang, L., Ching-Hui, T., Doo, W.-B., Ku, C.-Y., & Sibuet, J.-C. (2008). Turbidity currents, submarine landslides and the 2006 pingtung earthquake off sw taiwan. TAO: Terrestrial, Atmospheric and Oceanic Sciences, 19(6), 7. doi: https://doi.org/10.3319/TAO.2008.19.6.767(PT)
- Islam, M. A., & Imran, J. (2010). Vertical structure of continuous release saline and turbidity currents. *Journal of Geophysical Research: Oceans*, 115(C8). doi: https://doi.org/10.1029/2009JC005365
- Jameson, A., Schmidt, W., & Turkel, E. (1981). Numerical solution of the euler equations by finite volume methods using runge kutta time stepping schemes. In 14th fluid and plasma dynamics conference (p. 1259). doi: https://doi.org/10.2514/6.1981-1259
- Kameda, J., & Okamoto, A. (2021). 1-D inversion analysis of a shallow landslide triggered by the 2018 eastern iburi earthquake in hokkaido, japan. *Earth, planets, and space: EPS*, 73(1). doi: https://doi.org/10.1186/s40623-021-01443-y
- Komar, P. D. (1985). The hydraulic interpretation of turbidites from their grain sizes and sedimentary structures. *Sedimentology*, 32(3), 395-407. doi: https://doi.org/10.1111/j.1365-3091.1985.tb00519.x
- Kostic, S., & Parker, G. (2006). The response of turbidity currents to a canyon–fan transition: internal hydraulic jumps and depositional signatures. *Journal of Hydraulic Research*, 44(5), 631–653.
- Kuenen, P. H., & Migliorini, C. (1950). Turbidity currents as a cause of graded bedding. The Journal of Geology, 58(2), 91–127. doi: https://doi.org/10.1086/625710
- Lesshafft, L., Meiburg, E., Kneller, B., & Marsden, A. (2011). Towards inverse modeling of turbidity currents: The inverse lock-exchange problem. Computers & Geosciences, 37(4), 521-529.
- Ma, H., Parker, G., Cartigny, M., Viparelli, E., Balachandar, S., Fu, X., & Luchi,
 R. (2025). Two-layer formulation for long-runout turbidity currents: theory and bypass flow case. *Journal of Fluid Mechanics*, 1009, A19. doi:
 https://doi.org/10.1017/jfm.2025.246
 - Maiorana, M., Sulli, A., Marelli, M., & Agate, M. (2024). "geological characteriza-

tion of a potential co2 storage play in the gela offshore (southern sicily) and the role of a gravitational slide". *Marine and Petroleum Geology*, 170, 107127. doi: https://doi.org/10.1016/j.marpetgeo.2024.107127

- Mitra, R., Naruse, H., & Abe, T. (2020). Estimation of tsunami characteristics from deposits: Inverse modeling using a deep-learning neural network. *Journal of Geophysical Research: Earth Surface*, 125(9), e2020JF005583. doi: https://doi.org/10.1029/2020JF005583
- Mitra, R., Naruse, H., & Abe, T. (2024). Understanding flow characteristics from tsunami deposits at odaka, joban coast, using a deep neural network (dnn) inverse model. Natural Hazards and Earth System Sciences, 24 (2), 429–444. doi: https://doi.org/10.5194/nhess-24-429-2024
- Mitra, R., Naruse, H., & Fujino, S. (2021). Reconstruction of flow conditions from 2004 indian ocean tsunami deposits at the phra thong island using a deep neural network inverse model. *Natural Hazards and Earth System Sciences*, 21(5), 1667–1683. doi: https://doi.org/10.5194/nhess-21-1667-2021
- Moretti, L., Mangeney, A., Walter, F., Capdeville, Y., Bodin, T., Stutzmann, E., & Le Friant, A. (2020). Constraining landslide characteristics with bayesian inversion of field and seismic data. Geophysical journal international, 221(2), 1341–1348. doi: https://doi.org/10.1093/gji/ggaa056
- Nair, V., & Hinton, G. E. (2010). Rectified linear units improve restricted boltzmann machines. In *Proceedings of the 27th international conference on machine learning (icml-10)* (pp. 807–814).
- Nakao, K., Naruse, H., & Tokuhashi, S. (2020). Inverse analysis to reconstruct hydraulic conditions of non-steady turbidity currents: Application to an ancient turbidite of the kiyosumi formation of the awa group, boso peninsula, central japan. *Earth ArXiv*. doi: https://doi.org/10.31223/X51S3S
- Naruse, H. (2005). Usage and advantages of an application program 'stube' for settling tube grain-size analysis. *Journal of the Sedimentological Society of Japan*, 62(62), 55-61. doi: https://doi.org/10.4096/jssj1995.62.55
- Naruse, H. (2020). Numerical simulation of turbidity current by open source software "turb2d". *Journal of the Sedimentological Society of Japan*, 78(2), 54. doi: https://doi.org/10.4096/jssj.78.54
- Naruse, H., & Nakao, K. (2021). Inverse modeling of turbidity currents using an artificial neural network approach: verification for field application. Earth Surface Dynamics, 9(5), 1091–1109. doi: https://doi.org/10.5194/esurf-9-1091-2021
- Nezu, I. (2019). Hydraulics. Asakura Publishing Co., Ltd.
- Nygård, R., Gutierrez, M., Bratli, R. K., & Høeg, K. (2006). Brittle-ductile transition, shear failure and leakage in shales and mudrocks. *Marine and Petroleum Geology*, 23(2), 201-212. doi: https://doi.org/10.1016/j.marpetgeo.2005.10.001
- Ogata, Y., & Yabe, T. (1999). Shock capturing with improved numerical viscosity in primitive euler representation. *Computer Physics Communications*, 119(2), 179-193. doi: https://doi.org/10.1016/S0010-4655(99)00188-5
- Parker, G., Fukushima, Y., & Pantin, H. M. (1986). Self-accelerating turbidity currents. *Journal of Fluid Mechanics*, 171, 145–181. doi: https://doi.org/10.1017/S0022112086001404
- Parker, G., Garcia, M., Fukushima, Y., & Yu, W. (1987). Experiments on turbidity currents over an erodible bed. *Journal of Hydraulic Research*, 25(1), 123–147. doi: https://doi.org/10.1080/00221688709499292
- Parker, G., Toro-Escobar, C. M., Ramey, M., & Beck, S. (2003). Effect of floodwater extraction on mountain stream morphology. *Journal of Hydraulic Engineering*, 129(11), 885-895. doi: https://doi.org/10.1061/(ASCE)0733-9429(2003) 129:11(885)
- Parkinson, S. D., Funke, S. W., Hill, J., Piggott, M. D., & Allison, P. A. (2017).

Application of the adjoint approach to optimise the initial conditions of a turbidity current with the AdjointTurbidity 1.0 model. *Geoscientific Model Development*, 10(3), 1051–1068. doi: https://doi.org/10.5194/gmd-10-1051-2017

- Peakall, J., McCaffrey, B., & Kneller, B. (2000). A process model for the evolution, morphology, and architecture of sinuous submarine channels. *Journal of Sedimentary Research*, 70(3), 434-448. doi: https://doi.org/10.1306/2DC4091C-0E47-11D7-8643000102C1865D
- Piper, D. J., & Aksu, A. E. (1987). The source and origin of the 1929 grand banks turbidity current inferred from sediment budgets. Geo-Marine Letters, 7(4), 177–182. doi: https://doi.org/10.1007/BF02242769
- Piper, D. J., Cochonat, P., & Morrison, M. L. (1999). The sequence of events around the epicentre of the 1929 grand banks earthquake: initiation of debris flows and turbidity current inferred from sidescan sonar. Sedimentology, 46(1), 79–97. doi: https://doi.org/10.1046/j.1365-3091.1999.00204.x
- Polonia, A., Bonatti, E., Camerlenghi, A., Lucchi, R. G., Panieri, G., & Gasperini, L. (2013). Mediterranean megaturbidite triggered by the ad 365 crete earthquake and tsunami. Scientific reports, 3(1), 1285. doi: https://doi.org/ 10.1038/srep01285
- Poppeschi, J., Nakata, K., & Naruse, H. (2023). Conditions of submarine levéed channel inception: Examination by flume experiments. Sedimentology, 70(7), 2175–2195. doi: https://doi.org/10.1111/sed.13117
- Rowland, J. C., Hilley, G. E., & Fildani, A. (2010). A test of initiation of submarine leveed channels by deposition alone. *Journal of Sedimentary Research*, 80(8), 710–727. doi: https://doi.org/10.2110/jsr.2010.067
- Salinas, J. S., Cantero, M. I., Shringarpure, M., & Balachandar, S. (2019). Properties of the body of a turbidity current at near-normal conditions: 2. effect of settling. *Journal of Geophysical Research: Oceans*, 124(11), 8017–8035. doi: https://doi.org/10.1029/2019JC015335
- Sequeiros, O. E., Spinewine, B., Beaubouef, R. T., Sun, T., García, M. H., & Parker, G. (2010). Characteristics of velocity and excess density profiles of saline underflows and turbidity currents flowing over a mobile bed. *Journal of Hydraulic Engineering*, 136(7), 412-433. doi: https://doi.org/10.1061/(ASCE)HY.1943-7900.0000200
- Skevington, E. W., & Dorrell, R. M. (2025). Gravity current energetics and particle suspension. *Journal of Fluid Mechanics*, 1009, A30. doi: 10.1017/jfm.2025.285
- Spychala, Y. T., Eggenhuisen, J. T., Tilston, M., & Pohl, F. (2020). The influence of basin setting and turbidity current properties on the dimensions of submarine lobe elements. Sedimentology, 67(7), 3471-3491. doi: https://doi.org/10.1111/sed.12751
- Srivastava, N., Hinton, G., Krizhevsky, A., Sutskever, I., & Salakhutdinov, R. (2014). Dropout: a simple way to prevent neural networks from overfitting. *The journal of machine learning research*, 15(1), 1929–1958.
- Stevenson, C. J., Talling, P. J., Wynn, R. B., Masson, D. G., Hunt, J. E., Frenz, M., ... Cronin, B. T. (2013). The flows that left no trace: Very large-volume turbidity currents that bypassed sediment through submarine channels without eroding the sea floor. Marine and Petroleum Geology, 41, 186-205. (Special Issue: Internal architecture, bedforms and geometry of turbidite channels) doi: https://doi.org/10.1016/j.marpetgeo.2012.02.008
- Talling, P. J., Baker, M. L., Pope, E. L., Ruffell, S. C., Jacinto, R. S., Heijnen, M. S., . . . others (2022). Longest sediment flows yet measured show how major rivers connect efficiently to deep sea. *Nature Communications*, 13(1), 1–15. doi: https://doi.org/10.1038/s41467-022-31689-3
- Talling, P. J., Masson, D. G., Sumner, E. J., & Malgesini, G. (2012). Subaqueous sediment density flows: Depositional processes and deposit types. Sedimentol-

ogy, 59(7), 1937-2003. doi: https://doi.org/10.1111/j.1365-3091.2012.01353.x 1192 Yabe, T., & Wang, P.-Y. (1991).Unified numerical procedure for compressible 1193 and incompressible fluid. Journal of the Physical Society of Japan, 60(7), 2105-2108. doi: https://doi.org/10.1143/JPSJ.60.2105 A study on the water front in shal-Yang, H., Lu, M., & Kumakura, T. (2016).1196 low water equations. Journal of Japan Society of Civil Engineers, Ser. B1, Hy-1197 draulic Engineering, 72(4), I_325–I_330. doi: https://doi.org/10.2208/jscejhe 1198 $.72.I_{-}325$